Design criteria for ultrafast optical parametric amplifiers

Tutorial

Design criteria for ultrafast optical parametric amplifiers

C Manzoni and G Cerullo

Istituto di Fotonica e Nanotecnologie - Consiglio Nazionale delle Ricerche and Dipartimento di Fisica, Politecnico di Milano, Piazza L. da Vinci 32, 20133 Milano, Italy

E-mail: cristian.manzoni@polimi.it and giulio.cerullo@polimi.it

Abstract
Optical parametric amplifiers (OPAs) exploit second-order nonlinearity to transfer energy from a fixed frequency pump pulse to a variable frequency signal pulse, and represent an easy way of tuning over a broad range the frequency of an otherwise fixed femtosecond laser system. OPAs can also act as broadband amplifiers, transferring energy from a narrowband pump to a broadband signal and thus considerably shortening the duration of the pump pulse. Due to these unique properties, OPAs are nowadays ubiquitous in ultrafast laser laboratories, and are employed by many users, such as solid state physicists, atomic/molecular physicists, chemists and biologists, who are not experts in ultrafast optics. This tutorial paper aims at providing the non-specialist reader with a self-consistent guide to the physical foundations of OPAs, deriving the main equations describing their performance and discussing how they can be used to understand their most important working parameters (frequency tunability, bandwidth, pulse energy/repetition rate scalability, control over the carrier-envelope phase of the generated pulses). Based on this analysis, we derive practical design criteria for OPAs, showing how their performance depends on the type of the nonlinear interaction (crystal type, phase-matching configuration, crystal length), on the characteristics of the pump pulse (frequency, duration, energy, repetition rate) and on the OPA architecture.

(Some figures may appear in colour only in the online journal)

1. Introduction

Ultrafast optics has developed to be a major enabling technology in modern science, with many fundamental and real-world applications made possible by the ultrashort durations, high peak powers and broad bandwidths of femtosecond pulses [1]. While the first, seminal experiments were performed using 'liquid' dye-laser technology [2], which is unfriendly and with limited average power/pulse energy scaling capabilities, in the last two decades there has been a truly spectacular technological progress in ultrashort pulse generation from solid-state laser systems. Nowadays, reliable, rugged and power scalable sources of femtosecond pulses exist, mainly based on Ti:sapphire [3] or Yb:doped gain

media. While Ti:sapphire is a rather mature technology, Yb-based systems have still a huge development potential, in terms of both average and peak power [4–6]. The main limitation of such sources is that they operate at fixed wavelengths (800 nm for Ti:sapphire and 1040 nm for Yb) with modest tunability. Another specific drawback of Yb technology is the comparably narrow gain bandwidth, resulting in amplified pulses with typical duration of a few hundred femtoseconds. Fixed wavelength operation contrasts with the requirements of many applications, in time-resolved optical spectroscopy and high-field physics, which call for optical pulses with broadly tunable frequency. In femtosecond pump–probe spectroscopy, the system under study (be it of atomic, molecular or solid-state nature) is excited by a 'pump'
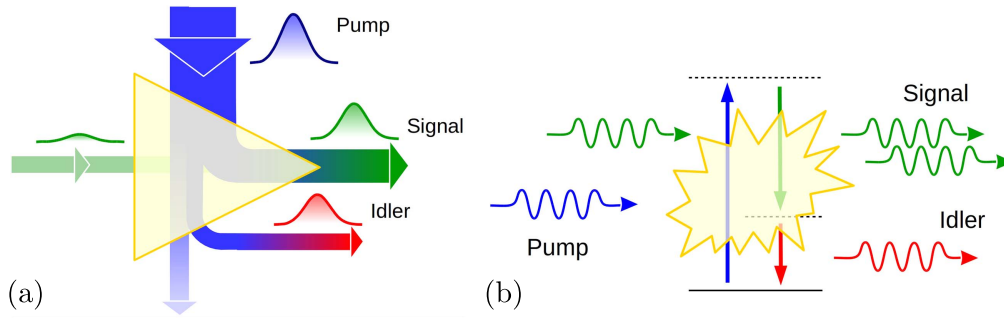
Figure 1. Optical parametric amplification can be visualized as: (a) power flow from an intense pump beam to a weak signal beam; (b) stimulated emission of signal photons from a virtual level excited by the pump photons.

pulse, resonant with a transition of the system, and its subsequent time evolution is monitored by measuring the pump-induced transmission change of a delayed 'probe' pulse [7]. The need to excite a system on resonance and probe optical transitions occurring at different photon energies requires broad frequency tunability of both pump and probe pulses [8]. Similar requirements on pulse tunability also apply to more advanced spectroscopic techniques, such as two-dimensional electronic and vibrational spectroscopy. In high-field processes such as high harmonic generation [9] the wavelength tunability of the driver pulses is important, since it influences both the energy cutoff of the XUV pulses and the phase-matching conditions of the process [10].

As there are no classical laser active media, based on population inversion, capable of providing gain over the required broad frequency range from the mid-infrared to the visible, frequency tunability must be achieved by a nonlinear optical effect, exploiting the very high peak powers produced by femtosecond sources. In most cases, frequency tunability is achieved by the second order nonlinear optical effect known as optical parametric amplification (OPA) [11, 12]. The principle of OPA is quite simple (figure 1(a)): in a suitable nonlinear crystal, energy is transferred from an high frequency and high intensity beam (the pump beam, at frequency ω_3) to a lower frequency, lower intensity beam (the signal beam, at frequency ω_1) which is thus amplified; in addition a third beam (the idler beam, at frequency ω_2) is generated, to fulfill energy conservation. The OPA process can be given a simple corpuscular interpretation, where interaction is similar to a collision of photons (see figure 1(b)): a photon at frequency ω_3 is absorbed by a virtual level of the material and a photon at frequency ω_1 stimulates the emission of two photons at frequencies ω_1 and ω_2. In this interaction, energy conservation

$$\hbar\omega_3 = \hbar\omega_2 + \hbar\omega_1 \qquad (1.1)$$

is fulfilled. The signal frequency to be amplified can vary in principle from 0 to ω_3, and correspondingly the idler varies from ω_3 to 0 (as a matter of fact, the lowest frequency is limited by absorption of the nonlinear crystal). The so-called degeneracy condition is achieved when $\omega_1 = \omega_2$. As will be discussed in the next section, the OPA process is efficient when, in addition to energy conservation, the phase-matching

condition $\Delta k = k_3 - k_2 - k_1 = 0$ is satisfied, where k_i are the wave vectors of the interacting beams.

In summary, the OPA process transfers energy from a high-power, fixed frequency pump beam to a low-power, variable frequency signal beam, generating an idler beam to satisfy energy conservation. The OPA can thus be seen as a 'photon cutter', cutting a high energy photon $\hbar\omega_3$ into the sum of two lower energy photons $\hbar\omega_1$ and $\hbar\omega_2$. The OPA process thus provides an optical amplifier with continuously variable frequency (determined by the phase-matching condition) and represents an easy way of tuning a fixed frequency femtosecond laser system. On the other hand, if suitably designed, an OPA can simultaneously fulfill the phase-matching condition for a very broad range of signal frequencies. The OPA thus acts as a broadband amplifier, efficiently transferring energy from a narrowband pump pulse to a broadband signal (idler) pulse; it can therefore be used to generate pulses significantly shorter—by more than an order of magnitude—than the pump pulse. This property of OPAs is especially important when they are combined with Yb-based laser systems, which, despite their favorable characteristics in terms of efficiency, reliability and average power scalability, generate relatively long pulses. The concept of broadband OPA is very flexible and can be applied to produce few-optical-cycle pulses over a very wide range of frequencies, provided that a broadband yet weak seed is available and the proper phase-matching conditions are identified [13]. An additional unique feature of OPAs is their capability of scaling the output energy, in combination with energetic picosecond pump pulses (5–50 ps duration) generated by solid-state gain media such as Nd-doped (or more recently Yb-doped) crystals/glasses. With a long pump pulse, in order to achieve efficient energy extraction, it is necessary to temporally match the seed pulsewidth with that of the pump by first stretching the seed pulse and then, after the amplification step, recompressing it back to its transform-limited (TL) duration. This scheme, which is very similar to the chirped pulse amplification [14] occurring in a real gain medium, is known as optical parametric chirped pulse amplification (OPCPA) [15] and is considered as the most promising route for energy/average power/repetition rate scaling of few-optical-cycle pulses [16–18].

For these reasons and due to their multifaceted advantages/applications, OPAs are nowadays ubiquitous in

ultrafast laser laboratories, coupled with pump lasers based on Ti:sapphire or, more recently, Yb technology. Many users who are not specialists in ultrafast optics, such as chemists, biologists, solid-state physicists and atomic/molecular physicists, are required to employ or, sometimes, even upgrade or develop OPAs for their research. A wide variety of configurations, operating in various spectral ranges, and with different pulse bandwidth, energy or repetition rate are possible. Despite the fact that many of these users are not specialists in ultrafast optics, they need to develop a good fundamental understanding of the physical principles underlying the operation of OPAs and of the parameters governing their performance, in order to be able to exploit these sources to their fullest for their application or even to design and build from scratch an OPA. The purpose of this tutorial paper is to provide the non-specialist reader with a self-consistent guide to the physical foundations of OPAs, deriving the main equations describing their performance and showing how they can be used to understand their most important working parameters (frequency tunability, bandwidth, pulse energy/ repetition rate scalability, control over the carrier-envelope phase (CEP) of the generated pulses...). These equations will then be used to derive practical design criteria for OPAs, showing how their performance depends on the type of the nonlinear interaction (crystal type, phase-matching configuration, crystal length), on the characteristics of the pump pulse (frequency, duration, energy, repetition rate,...) and on the OPA architecture (single *versus* multi-stage, collinear *versus* non-collinear,...). Once the basic principles governing OPA operation are understood, the interested reader is referred to the vast amount of technical literature describing in detail the architecture and parameters of specific OPA configurations. The paper is organized as follows: in section 2 we introduce the basic concepts of optical parametric amplification, such as phase matching, polarisation schemes, and energy conservation. We first focus on the interaction of monochromatic waves, and then extend some of these concepts to the amplification of broadband pulses. In this case, we also introduce the non-collinear interaction geometry and discuss the amplification bandwidth and the importance of the crystal length. Finally, we discuss the spectral and phase properties of the idler beam. Based on these results, in section 3 we provide practical design criteria for ultrafast OPAs. After introducing the basic building blocks of an OPA, we discuss the main techniques to generate the broadband seed, and the dependence of the OPA performances on the pump-pulse characteristics. We also discuss the concept of dispersion, and describe some of the main techniques that can be used for pulse compression. For each of these aspects, we provide the reader with some design criteria, a list of suggestions to take into account when building an OPA.

2. Second-order interactions in nonlinear crystals

In order to highlight the main factors influencing the optical parametric amplification process with ultrashort pulses, we will give a brief theoretical treatment of ultrafast nonlinear optics [19, 20]. We start with a linearly polarized plane wave $E(z, t)$ which—during propagation in a medium in direction z —induces a polarisation

$$P(z, t) = P_{\mathrm{L}}(z, t) + P_{\mathrm{NL}}(z, t). \qquad (2.1)$$

Here, $P_{\mathrm{L}}(z, t)$ is the linear polarisation and $P_{\mathrm{NL}}(z, t)$ the nonlinear term induced by strong electric fields, and depending on E^2, E^3,...

According to Maxwell's equations, written in the scalar approximation, the evolution of the field can be described by:

$$\frac{\partial^2 E(z, t)}{\partial z^2} - \mu_0 \frac{\partial^2 D(z, t)}{\partial t^2} = \mu_0 \frac{\partial^2 P_{\mathrm{NL}}(z, t)}{\partial t^2}, \qquad (2.2)$$

where $D(z, t) = \varepsilon_0 E(z, t) + P_{\mathrm{L}}(z, t)$ is the electric displacement field due to the linear polarisation of the material (see equation (A.9)), and μ_0 is the magnetic permeability of vacuum.

With very strong interacting fields, $\partial^2 P_{\mathrm{NL}}(z, t)/\partial t^2$ acts as a source term, and is responsible for a rich variety of physical effects arising from its nonlinear dependence on $E(z, t)$.

In this paper we will limit our analysis to second order effects and neglect the dependence of the nonlinear polarisation on $E^3(z, t)$ and higher orders, thus writing:

$$P_{\mathrm{NL}}(z, t) = \varepsilon_0 \chi^{(2)} E^2(z, t) = 2\varepsilon_0 d_{\mathrm{eff}} E^2(z, t). \qquad (2.3)$$

Here d_{eff} is the so-called effective nonlinear optical coefficient which depends on the specific components of the second-order nonlinear tensor $\chi^{(2)}$ involved in the interaction. Such a situation is known as *nonlinear second-order parametric process* and, when fields with different frequencies (carrier waves) simultaneously propagate in a nonlinear medium, leads to an exchange of energy between them. Due to the tensorial nature of nonlinear interaction, such energy exchange may also occur among fields with different polarisation states and propagation directions, as will be discussed in section 2.2.

When $P_{\mathrm{NL}}(z, t)$ is negligible, $E(z, t)$ experiences *linear propagation*, which is described in detail in appendix A. On the other hand, when the field $E(z, t)$ is strong enough to induce a nonlinear polarisation $P_{\mathrm{NL}}(z, t)$, *nonlinear processes* take place. For the case of the OPA process, it is convenient to write $E(z, t)$ as a superposition of three fields with different carrier frequencies, the pump, signal and idler fields. The nonlinear process is responsible for their interactions and energy exchange. The solution of equation (2.2) is not straightforward, and many methods, both numerical [21] and analytical [22], have been proposed to describe various interaction regimes under different boundary conditions. However, many of the general properties of optical parametric amplification can be derived from the approximate solutions of the differential equation. Such solutions constitute powerful tools for the design of OPAs and provide important physical insight into the parameters governing their performance. In the following we will therefore start from equation (2.2) to separately focus on:

(i) *Parametric amplification of monochromatic waves*: since a light pulse is, according to the Fourier theorem (see appendix A.1), a superposition of monochromatic waves, we will start by studying the nonlinear second-order interaction between monochromatic waves, focusing on *the OPA process*. The particular case of monochromatic interaction will allow us to introduce the basic concept of *phase-matching*.

(ii) *Broadband parametric amplification*: broadband amplification will be studied by extending the phase-matching concept from the monochromatic to the broadband case.

We will consider the process in a nonlinear birefringent medium; the interacting fields will be three co-propagating plane waves, namely the signal $E_1(z, t)$, the idler $E_2(z, t)$ and the pump $E_3(z, t)$.

2.1. Parametric amplification of monochromatic waves

In this section we will discuss the nonlinear interaction among *monochromatic* waves propagating in a a non-centrosymmetric medium; to this aim, we will consider three fields, at angular frequencies ω_1, ω_2 and ω_3. If the three waves co-propagate along the z-direction, the resulting electric field is (see equation (A.3)):

$$
\begin{aligned}
E(z, t) = \frac{1}{2} \{ & A_1(z) e^{j(\omega_1 t - k_1 z)} \\
& + A_2(z) e^{j(\omega_2 t - k_2 z)} + A_3(z) e^{j(\omega_3 t - k_3 z)} \} + \text{c.c.},
\end{aligned}
$$

$$(2.4)$$

where complex coefficients A_i and the relative dielectric constant ε_r (see equation (A.9)) do not depend on time as we are in the monochromatic regime. The corresponding nonlinear second order polarisation P_{NL}, calculated according to equation (2.3), contains components at frequencies $2\omega_1$, $2\omega_2$, $2\omega_3$ (second harmonic generation, SHG), $\omega_1 + \omega_2$, $\omega_1 + \omega_3$, $\omega_2 + \omega_3$ (sum frequency generation, SFG) and $\omega_3 - \omega_1$, $\omega_3 - \omega_2$, $\omega_2 - \omega_1$ (difference frequency generation, DFG). We will now assume that only those nonlinear interactions involving frequencies ω_1, ω_2 and ω_3 will efficiently take place, because the others do not satisfy the phase-matching condition, as will be discussed later. We will therefore consider the components of the nonlinear polarisation at frequencies $\omega_1 + \omega_2 (=\omega_3)$, $\omega_3 - \omega_2 (=\omega_1)$ and $\omega_3 - \omega_1 (=\omega_2)$, and reject all the other components. The resulting nonlinear polarisation is:

$$
\begin{aligned}
P_{\text{NL}}(z, t) = \; & \varepsilon_0 d_{\text{eff}} A_2^*(z) \cdot A_3(z) \cdot e^{j[\omega_1 t - (k_3 - k_2)z]} \\
& + \varepsilon_0 d_{\text{eff}} A_1^*(z) \cdot A_3(z) \cdot e^{j[\omega_2 t - (k_3 - k_1)z]} \\
& + \varepsilon_0 d_{\text{eff}} A_1(z) \cdot A_2(z) \cdot e^{j[\omega_3 t - (k_1 + k_2)z]} + \text{c.c.}
\end{aligned}
$$

$$(2.5)$$

and the forcing term $\partial^2 P_{\text{NL}}/\partial t^2$ is therefore:

$$
\begin{aligned}
\frac{\partial^2 P_{\text{NL}}(z, t)}{\partial t^2} = \; & -\varepsilon_0 d_{\text{eff}} \omega_1^2 A_2^*(z) \cdot A_3(z) \cdot e^{j[\omega_1 t - (k_3 - k_2)z]} \\
& - \varepsilon_0 d_{\text{eff}} \omega_2^2 A_1^*(z) \cdot A_3(z) \cdot e^{j[\omega_2 t - (k_3 - k_1)z]} \\
& - \varepsilon_0 d_{\text{eff}} \omega_3^2 A_1(z) \cdot A_2(z) \cdot e^{j[\omega_3 t - (k_1 + k_2)z]} + \text{c.c}
\end{aligned}
$$

$$(2.6)$$

This equation shows that:

- the nonlinear polarisation at one frequency is proportional to the product of the electric fields at the other two frequencies, so that the waves become nonlinearly coupled;
- the wavenumber of the nonlinear polarisation at a given frequency does not coincide with that of the corresponding wave.

By substituting the forcing term of equation (2.6) into (2.2), splitting the frequency components in three equations, and applying the *slowly varying envelope approximation* [23]:

$$
\left| \frac{\partial^2 A}{\partial z^2} \right| \ll 2k \left| \frac{\partial A}{\partial z} \right|
$$

$$(2.7)$$

we get the *coupled* wave equations [24]:

$$
\begin{cases}
\dfrac{\partial A_1}{\partial z} = -j\sigma_1 A_2^* A_3 \cdot e^{-j\Delta k z}, \\[2mm]
\dfrac{\partial A_2}{\partial z} = -j\sigma_2 A_1^* A_3 \cdot e^{-j\Delta k z}, \\[2mm]
\dfrac{\partial A_3}{\partial z} = -j\sigma_3 A_1 A_2 \cdot e^{j\Delta k z},
\end{cases}
$$

$$(2.8)$$

where $\sigma_i = d_{\text{eff}} \omega_i / c_0 n_i$, $n_i = \sqrt{\varepsilon_{\text{ri}}}$ is the refractive index, and $\Delta k = k_3 - k_2 - k_1$. This last parameter is called *wave–vector mismatch*: it determines the energy flow among the beams, and will be discussed in detail in the following sections. Note that the first two equations are formally identical, indicating that the fields at ω_1 and ω_2 play the same role.

According to the boundary initial conditions $A_i(0)$ ($i = 1, 2, 3$), two main processes can arise: SFG and DFG. In SFG the input fields are $A_1(0)$ and $A_2(0)$ at ω_1 and ω_2; their interaction produces A_3 at frequency $\omega_3 = \omega_1 + \omega_2$ (SHG is just a particular case in which $\omega_1 = \omega_2$). In DFG, the interaction initially involves fields $A_3(0)$ at ω_3 and $A_1(0)$ at ω_1; the field A_3 loses energy in favor of A_1 and of the newly generated A_2 at $\omega_2 = \omega_3 - \omega_1$. When $\omega_3 \approx \omega_1$, the limit process is called optical rectification, a process that is used in the generation of THz pulses [25].

OPA is a mechanism similar to DFG, except for the strength of the interacting fields: DFG arises when the fields at ω_3 and ω_1 have comparable intensities, while OPA occurs when the field at ω_1 is much weaker. In the OPA process, therefore, an intense beam at ω_3 (*pump*) transfers energy to
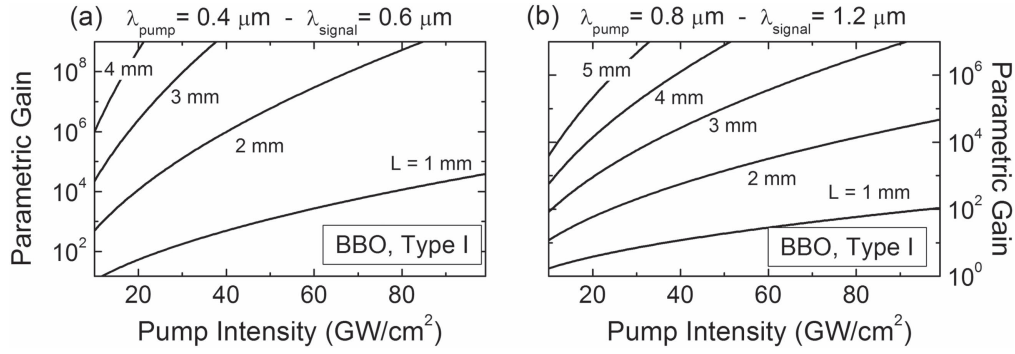
Figure 2. Parametric gain in a Type-I BBO crystal for various crystal lengths and pump intensities; the signal is (a) in the visible and (b) in the infrared.

the beam at ω_1 (*signal*), thereby amplifying it, and generates light at ω_2 (*idler*).

The same processes occur if DFG and OPA initially involve fields $A_3(0)$ at ω_3 and $A_2(0)$ at ω_2; in this case the newly generated field is A_1 at $\omega_1 = \omega_3 - \omega_2$. In parametric amplification this means that the concepts of signal and idler could be interchanged, with relevant consequences that will be explained later in this section.

Let's now solve equation (2.8) for the case of parametric amplification. We will make the assumption that the pump field is not depleted during the interaction ($A_3 \approx$ const.), and that there is no initial idler beam ($A_{20} = 0$). After proper manipulation, the signal evolution along the nonlinear medium is described by:

$$\frac{\partial^2 A_1}{\partial z^2} = -j\Delta k \frac{\partial A_1}{\partial z} + \Gamma^2 A_1$$
$$\text{with} \qquad \Gamma^2 = \frac{2d_{\text{eff}}^2 \omega_1 \omega_2}{c_0^3 \varepsilon_0 n_1 n_2 n_3} I_3, \qquad (2.9)$$

where the beam intensity is calculated as $I = n\varepsilon_0 c_0 \langle E(t)^2 \rangle = 1/2 \cdot n\varepsilon_0 c_0 |A|^2$ according to equation (A.4). We can also define a figure of merit (FM) for the OPA process as:

$$\text{FM} = \frac{d_{\text{eff}}^2}{n_1 n_2 n_3} \qquad (2.10)$$

which accounts for the linear and the nonlinear properties of the crystal.

After the interaction length L, the signal and idler intensities are:

$$\begin{cases} I_1(L) = I_{10} \left\{ 1 + \left[\frac{\Gamma}{g} \sinh(gL) \right]^2 \right\}, \\ I_2(L) = I_{10} \frac{\omega_2}{\omega_1} \left[\frac{\Gamma}{g} \sinh(gL) \right]^2, \end{cases} \qquad (2.11)$$

where

$$g = \sqrt{\Gamma^2 - \frac{\Delta k^2}{4}} \qquad (2.12)$$

is the *small-signal gain*. We can define the parametric gain $G(L)$ of the process as:

$$G(L) = \frac{I_1(L)}{I_{10}} = \left\{ 1 + \left[\frac{\Gamma}{g} \sinh(gL) \right]^2 \right\}. \qquad (2.13)$$

The gain strongly depends on g: its maximum value is obtained when $\Delta k = 0$, the so-called *phase-matching* condition.

In the large-gain limit ($gL \gg 1$):

$$I_1(L) \simeq I_{10} \left(\frac{\Gamma}{g} \right)^2 \frac{e^{2gL}}{4}$$
$$I_2(L) \simeq I_{10} \frac{\omega_2}{\omega_1} \left(\frac{\Gamma}{g} \right)^2 \frac{e^{2gL}}{4}$$
$$G(L) \simeq \left(\frac{\Gamma}{g} \right)^2 \frac{e^{2gL}}{4} \qquad (2.14)$$

which show that, within the no-depletion approximation, both signal and idler intensities grow exponentially with the interaction length L. An example of calculation of the parametric gain G as a function of pump intensity for different interaction lengths is shown in figure 2, where we used the nonlinear coefficient d_{eff} and the refractive indexes of a Type-I interaction in β-barium borate (β-BaB$_2$O$_4$, or BBO). Note that this calculation, performed for monochromatic waves and neglecting pump depletion, gives the upper limit for the parametric gain. For amplification of short light pulses, the gain is further limited by the energy stored in the pump and the initial energy of the seed, by the temporal overlap of pump, signal and idler pulses and by the parasitic absorption of the nonlinear medium; the role of these parameters will be discussed in detail in sections 2.3 and 3.3.

The exponential growth of the gain with propagation length is qualitatively different from the quadratic growth that occurs in other second-order processes like SFG and SHG [19, 20] and shows that the OPA behaves like a real amplifier. With respect to a classical optical amplifier based on population inversion in an atomic or molecular transition, however, an OPA has three important differences:
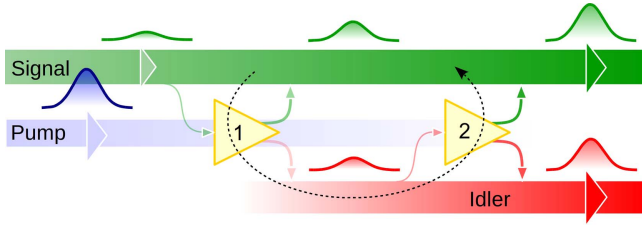
Figure 3. Scheme of the positive feedback mechanism occurring in an OPA and giving rise to the exponential parametric gain. Here we show two of the infinite local interactions occurring in an OPA. Amplifier 2 contributes to the signal amplification through the interaction with the idler generated by Amplifier 1. The resulting feedback is the dashed arrow.

(i) it does not have any energy storage capability, i.e. the gain is present only during the temporal overlap of the interacting pulses;

(ii) the gain center frequency is not fixed, but can be continuously adjusted by varying the phase-matching condition;

(iii) the gain bandwidth is not limited by the linewidth of an electronic/vibration transition, but rather by the possibility of satisfying the phase-matching condition over a broad range of frequencies.

Let us now consider the factors influencing the parametric gain G:

- G strongly depends on the parameter g, which is maximum when

$$\Delta k = k_3 - k_2 - k_1 = 0 \qquad \text{(phase matching)} \qquad (2.15)$$

  G rapidly decreases for non-zero values of Δk, indicating that phase matching is a key condition to be fulfilled in order to get significant amplification from the nonlinear material. In the following we will focus on the case $\Delta k = 0$, leading to $g = \Gamma$.

- According to the definition of g, G depends exponentially on the square root of the figure of merit FM (see equation (2.10)): for high efficiency one should therefore select the crystal with the highest FM, or at least the largest d_{eff}. There are however other considerations leading to the choice of the crystal, such as the range of phase-matchable frequencies, dispersion properties, availability and optical damage threshold.

- The gain G scales also as the exponential of the square root of the pump intensity I_3. In the pulsed regime, the highest intensity is at the pulse peak, and depends on the pulse duration, its energy and the beam size. This indicates the suitability of ultrashort pulses for pumping OPAs, due to their high peak powers.

- The parametric gain scales as the exponential of the crystal length L. This gain is strikingly different from the efficiency of SHG/SFG, which scales as the square of the crystal length: during the nonlinear interaction the idler beam is generated at the difference frequency between pump and signal. Thanks to the symmetry between A_1 and A_2 (see equation (2.8)), also the idler can undergo

parametric amplification and a beam at the signal frequency and phase is generated, thus adding power to the amplified seed. This mechanism acts as positive feedback giving rise to an exponential gain of the signal during its propagation [19], as sketched in figure 3. The energy exchange with the idler is so vital for parametric amplification, that if the idler beam spatially or temporally walks off from the pump, is absorbed by the nonlinear medium, or is depleted by other parasitic processes, the gain of the OPA is dramatically reduced. For this reason, absorption of the idler influences the tunability range of the OPA, as we will discuss in section 3.3.1.

- G scales as the exponential of the square root of the product of signal and idler frequencies. This seems to indicate an advantage to use high pump frequencies. However we will see that with ultrashort pulses this advantage is often offset by the larger difference in group velocities of the interacting pulses, which force to use shorter crystals and thus decrease gain.

2.1.1. Energy and momentum conservation. It is worthwhile mentioning that the phase-matching condition $k_3 = k_2 + k_1$ (equation (2.15)) arising from the coupled equations, and the relationship between the frequencies $\omega_3 = \omega_2 + \omega_1$, can both be rewritten as:

$$\hbar k_3 = \hbar k_2 + \hbar k_1, \qquad (2.16)$$

$$\hbar \omega_3 = \hbar \omega_2 + \hbar \omega_1 \qquad (2.17)$$

which represent momentum and energy conservation for the interacting pump, signal and idler photons in the corpuscular interpretation of parametric processes. In the following section, we will give an interesting interpretation to both these equations.

2.1.2. Manley–Rowe equations. By suitably manipulating the coupled equation (2.8), we can get the following intensity equations:

$$\frac{1}{\omega_1} \frac{\partial I_1}{\partial z} = \frac{1}{\omega_2} \frac{\partial I_2}{\partial z} = -\frac{1}{\omega_3} \frac{\partial I_3}{\partial z}. \qquad (2.18)$$

These equations are known as *Manley–Rowe relations*; they were developed originally to predict energy conservation in a nonlinear electric circuit [26], and then extended to other fields, including nonlinear optics [24]. As a consequence, if we express the beam intensity $I_i(z)$ as a function of the flux of photons $N_i(z)$ crossing the unit surface S per unit time Δt:

$$I_i(z) = \frac{N_i(z) \cdot \hbar \omega_i}{S \Delta t} c_0 \qquad (2.19)$$

equation (2.18) gives:

$$\frac{\partial N_1(z)}{\partial z} = \frac{\partial N_2(z)}{\partial z} = -\frac{\partial N_3(z)}{\partial z}. \qquad (2.20)$$

This relationship shows that a second order parametric interaction involves three photons, one from each frequency:
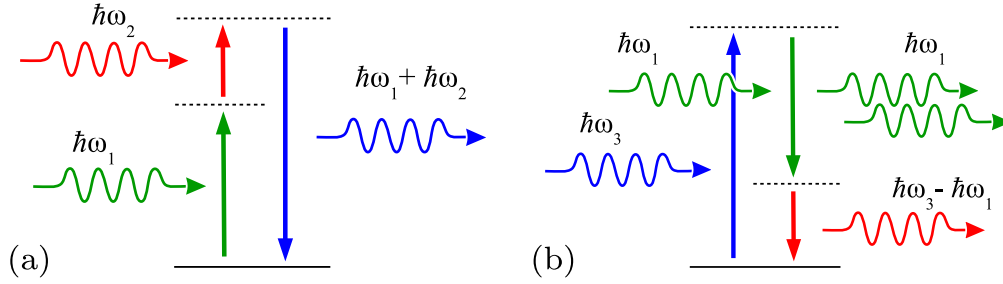
Figure 4. Simple models of second order nonlinear interactions based on excitation of virtual levels for (a) sum frequency generation and (b) optical parametric amplification.

according to the process and the initial conditions, each photon can be absorbed or emitted.

A picture of parametric effects based on photon absorption and emission from virtual levels of a nonlinear medium is depicted in figure 4. In the case of SFG, when the two photons at ω_1 and ω_2 are absorbed, they instantaneously excite the material to a high energy virtual level. The decay from this level produces the emission of a photon at $\omega_3 = \omega_1 + \omega_2$. Similarly, in an OPA absorption of a pump photon at ω_3 drives the material into the virtual excited state. A signal photon at ω_1 can stimulate a decay towards an intermediate state, thus giving rise to a new signal photon, with the same phase as the stimulating one; this is the mechanism of amplification. An idler photon at ω_2 is then emitted in order to complete the decay towards the ground state.

Since the response of the material is instantaneous, a parametric interaction occurs only when two photons cross together the same volume of the medium, and can be seen as a collision between photons. Since the collision probability depends on the number of photons, nonlinear processes require intense beams to take place efficiently.

2.1.3. Phase matching. A very important parameter which, together with the crystal nonlinearity d_{eff}, determines the efficiency of a second order nonlinear interaction, is the phase mismatch $\Delta k = k_3 - k_2 - k_1$. We have already seen that the interaction is optimized when $\Delta k = 0$, at perfect *phase matching*: we will now discuss the physical meaning of this condition.

We first start from an *undulatory* point of view. During a nonlinear process, new frequencies are generated *locally* in the material, and then propagate with their own phase velocity. This process takes place at all longitudinal coordinates inside of the material, so that during propagation along the medium the new components superpose on each other, giving rise to an interference which is generally destructive and leads to negligible macroscopic nonlinear effects, even in the presence of strong fields. To observe a macroscopic net effect, the phase velocities of the nonlinearly generated fields should be tuned so that they can constructively interfere during propagation: in particular the propagation speed of the forcing term $\partial^2 P_{\text{NL}}/\partial t^2$ should be equal to the phase velocity of the nonlinearly generated beam, so that the components generated in different points of the crystal
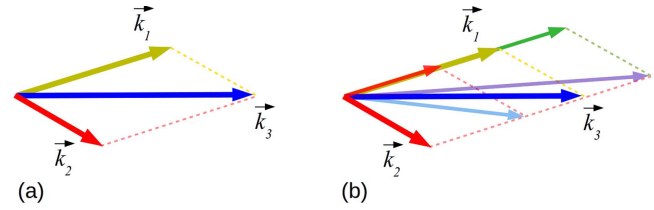

Figure 5. (a) SFG scheme in a non-collinear configuration. (b) effects of the detuning of one of the beams' frequency on the propagation direction of the SFG beam.

share the same phase and experience constructive interference.

Considering for example the SFG process, we know from equation (2.6) that the forcing term due to the nonlinear polarisation ($\partial^2 P_{\text{NL}}/\partial t^2$) and the SFG beam at ω_3 propagate as

$$e^{j[\omega_3 t - (k_1 + k_2)z]} \quad \text{and} \quad e^{j(\omega_3 t - k_3 z)}. \quad (2.21)$$

The phase velocities of these fields are

$$v_{P_{\text{NL}}} = \frac{k_1 + k_2}{\omega_3} \quad \text{and} \quad v_3 = \frac{k_3}{\omega_3} \quad (2.22)$$

so that phase–velocity matching occurs when

$$k_3 = k_1 + k_2 \quad (2.23)$$

corresponding to the phase-matching condition. If nonlinear interactions are described as collisions of photons, the *corpuscular* interpretation of phase matching is momentum conservation during such collisions. This picture is particularly useful because it allows us to easily extend the phase-matching condition to the vectorial case, which occurs when the interacting beams are non-collinear; momentum conservation leads to a vectorial equation:

$$\hbar \vec{k}_3 = \hbar \vec{k}_2 + \hbar \vec{k}_1 \quad \text{momentum conservation,} \quad (2.24)$$

$$\vec{k}_3 = \vec{k}_2 + \vec{k}_1 \quad \text{non-collinear phase matching.} \quad (2.25)$$

From this condition, we can also deduce the propagation direction of the beam generated by the non-collinear interaction of two fields. As an example, in figure 5 we show non-collinear SFG between two beams with $\vec{k}_1$ and $\vec{k}_2$. The propagation direction $\vec{k}_3$ of the beam at the sum-frequency is given by the phase-matching condition. This also shows that tuning one of the beams changes the propagation direction of the sum-frequency field.
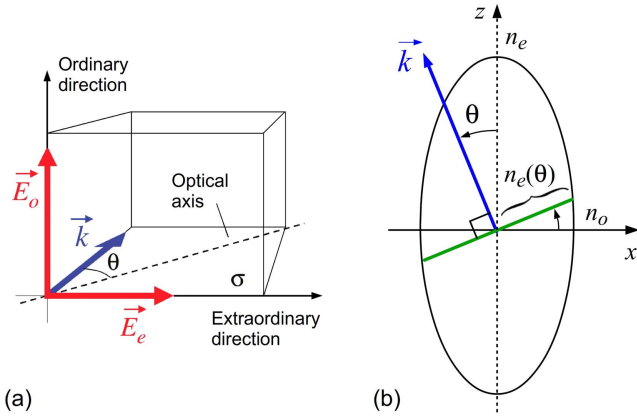
Figure 6. (a) ordinary and extraordinary directions in uniaxial birefringent crystals. (b) Section of the index ellipsoid and graphical meaning of the extraordinary refractive index, for a positive uniaxial crystal. The optical axis is in the z-direction.

We note that both the wave and corpuscular interpretations of phase-matching, including the non-collinear interaction, can be easily extended to the DFG process occurring during parametric amplification. We will often refer to these models for the design of an OPA, as explained in the following sections.

2.2. Interaction types

In section 2.1 we introduced the differential equations describing the nonlinear interaction between pump, signal and idler monochromatic fields assuming the same propagation directions and without specifying the polarisation of the beams (see equation (2.4)). In general, the interaction involves fields with different polarisations and different propagation directions; a complete description of second-order processes accounting for the polarisations of the fields through the nonlinear susceptibility tensor goes beyond the scope of this paper. However, it is possible to derive the main properties of OPA by extending some of the results discussed so far to the general case of non-collinear beams, with different polarisations.

To take polarisation of the fields into account, it is sufficient to reduce the nonlinear susceptibility tensor to the scalar coefficient d_{eff} (see equation 2.3), which accounts for the average interaction strength among the fields. To study the interaction types based on the polarisation states of the fields, we will limit ourselves in this paper to the simpler, and more commonly adopted, uniaxial birefringent crystals; the reader is referred to [27, 28] for a complete treatment of birefringence through the index ellipsoid and of the more general case of biaxial crystals. In uniaxial crystals, the best reference frame to describe the electric field of an electromagnetic wave is defined by the optical axis of the medium and the wave–vector $\vec{k}$ of the propagating beam. As sketched in figure 6, the optical axis and the wave–vector $\vec{k}$ define a plane σ and two normal directions, called ordinary (o) and extraordinary (e): these directions are a good reference frame to define the

Table 1. Summary of polarisation configurations in second order processes.

Type	ω_3 extraordinary	ω_3 ordinary
Type 0	eee	ooo
Type I	ooe	eeo
Type II	eoe	eoo
	oee	oeo

polarisation state of the field. According to the most common classification of the polarisation configurations of the three interacting fields, we group them in the following interaction types (see table 1):

Type 0 The three interacting waves have equal polarisation states, either ordinary (ooo) or extraordinary (eee).

Type I The low-frequency fields (ω_1, ω_2) propagate with the same polarisation, either ordinary or extraordinary. The resulting configurations are therefore ooe or eeo, respectively.

Type II The low-frequency fields are cross-polarized, and the possible configurations are eoe, oee, eoo, oeo.

From the polarisation configuration of the fields it is possible to evaluate the two important parameters governing the nonlinear interaction: the nonlinear effective coefficient d_{eff}, which accounts for the second-order nonlinear response of the medium, and the frequency-dependent wave–vector mismatch Δk, which determines the efficiency of the energy flow between the interacting fields. Details on the nonlinear coefficient will be given in the appendix B.3; phase matching will be discussed in the following.

2.2.1. Phase-matching calculation. Let us now focus on the wave–vector mismatch Δk, the most important parameter in the nonlinear processes, which determines the efficiency of the energy flow between the interacting fields. In the case of the collinear interaction studied in section 2.1, the phase-matching condition can be expressed as a scalar equation:

$$\Delta k = k_3 - k_2 - k_1 = 0. \tag{2.26}$$

In the more general case of the fields propagating along different directions, i.e. in the non-collinear interaction geometry, momentum conservation becomes a vectorial equation:

$$\Delta \vec{k} = \vec{k}_3 - \vec{k}_2 - \vec{k}_1 = 0. \tag{2.27}$$

Note that the non-collinear configuration adds one degree of freedom, which allows to find a more favorable phase-matching condition; in parametric amplification, this is the angle between pump and signal, which also allows to spatially separate the three beams after amplification. The resulting non-collinear OPA is therefore also called NOPA [29].

In the following we will show how to obtain the phase-matching condition for the interaction among three *monochromatic* waves; we will first study the collinear case, and then extend the results to non-collinear geometry.

Collinear phase matching. In the collinear configuration, recalling that $k = \omega n/c_0$, the phase-matching condition is equivalent to

$$n_3 \omega_3 - n_2 \omega_2 - n_1 \omega_1 = 0 \qquad (2.28)$$

which links the refractive indexes n_i seen by the interacting beams and allows to refer to phase-matching also as *index matching*. In general, fulfilling this condition is not straightforward: equation (2.28) can be written

$$\omega_3 n_3 = \omega_1 n_1 + (\omega_3 - \omega_1) n_2$$
$$\rightarrow \omega_3 (n_3 - n_2) = \omega_1 (n_1 - n_2). \qquad (2.29)$$

If we assume that $\omega_1 < \omega_2 < \omega_3$, in isotropic media with positive dispersion ($\partial n/\partial \omega > 0$) the refractive indexes are $n_1 < n_2 < n_3$. Hence $n_3 - n_2 > 0$ and $n_1 - n_2 < 0$ and equation (2.29) has no solution. This shows that phase (index) matching is not obtainable in isotropic media with positive dispersion; the same conclusion holds in the presence of negative dispersion. To solve this problem, two approaches can be followed:

(i) exploit *birefringence* by propagating the beams with different polarisations, leading to Type-I and Type-II interaction schemes;

(ii) apply a periodic modulation to the sign of the nonlinear coefficient d_{eff}, leading to the so-called *quasi-phase-matching* (QPM) regime [30]; in this case the fields can propagate with parallel polarisation (Type 0). Phase matching is not locally satisfied, but the modulation of the sign of d_{eff} leads to an average macroscopic net exchange of energy between the fields.

To study phase matching by *birefringence*, for simplicity we will limit ourselves to uniaxial crystals. These crystals have two frequency-dependent refractive indexes: the ordinary index n_o and the extraordinary index n_e; if $n_o < n_e$, the crystal is called *positive* uniaxial crystal, whereas if $n_o > n_e$ it is called *negative* uniaxial crystal. The refractive index seen by a beam propagating in the crystal depends on its propagation direction and its polarisation, which can be either ordinary or extraordinary. Figure 6(a) shows how to identify these two privileged directions.

The ordinary polarisation propagates with index of refraction n_o, while the index of refraction experienced by the extraordinary polarisation varies from n_o to n_e as a function of the propagation angle θ. Figure 6(b) shows the pictorial meaning of $n_e(\theta)$: it is calculated from the intersection between the normal to the wave–vector $\vec{k}$ and the function $z^2/n_e^2 + x^2/n_o^2 = 1$, which is a section of the index ellipsoid [28]. The dependence of $n_e(\theta)$ on the propagation direction is given by:

$$\frac{1}{n_e(\theta)^2} = \frac{\cos^2 \theta}{n_o^2} + \frac{\sin^2 \theta}{n_e^2}. \qquad (2.30)$$

In this way, it is often possible to find one value of the propagation direction θ giving the right n_e which fulfills the phase-matching condition of equation (2.28). This angle is indicated with θ_m and is called phase-matching angle.
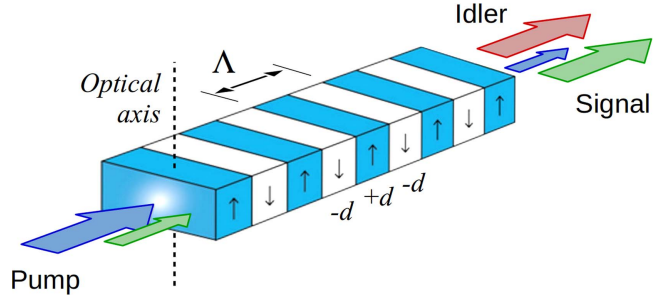

Figure 7. Sketch of a periodically poled crystal and the propagating fields of an OPA.

If only one field has extraordinary polarisation, θ_m can be exactly calculated from equations (2.28) and (2.30). Unfortunately, this calculation is not straightforward if two fields have extraordinary polarisation: some methods for the calculation of the phase-matching angle are illustrated in appendix B.

It is possible to show that not all the configurations listed in table 1 can be phase-matched. In particular, in negative uniaxial crystals ($n_e < n_o$), phase matching will never be obtained if ω_3 is ordinary. Similarly, phase matching will not occur if ω_3 is extraordinary in positive uniaxial media ($n_e > n_o$). For instance BBO, which is one of the most widespread nonlinear media, is a negative uniaxial crystal; hence, phase matching in BBO can be achieved only if ω_3 has extraordinary polarisation.

The second approach to obtain phase-matching, QPM, is typically used with those nonlinear crystals whose $\chi^{(2)}$ tensor is such that the highest nonlinear coefficient occurs when the three interacting beams have the same polarisations, as for stoichiometric lithium tantalate (SLT) or lithium niobate (LiNbO$_3$, LN). In these crystals the largest element of the nonlinear tensor is d_{33}, which contributes to the nonlinear process when the three interacting beams share the same extraordinary polarisation (Type 0 configuration). In this case birefringence phase-matching can never be obtained, as we discussed. However, it is still possible to benefit from such high nonlinearity by QPM, which is obtained by placing the optical axis of the crystal at an angle $\theta = 90°$ with respect to the wave–vectors, and spatially modulating the nonlinear properties of the medium [31]. This is achieved by periodically changing the sign of the $\chi^{(2)}$ coefficient, reversing the alignment of the ferroelectric domains in the crystal upon application of a suitable voltage, as shown in figure 7. When the modulation of the nonlinear coefficient is periodic, we introduce the modulation period Λ and the corresponding grating wave–vector $K_g = 2\pi/\Lambda$. The phase matching equation now includes the grating wave–vector and reads:

$$\Delta k = k_3 - k_2 - k_1 - K_g = 0. \qquad (2.31)$$

Finding the phase-matching condition, in this case, corresponds to calculating the poling period Λ_m. Note that, compared with phase-matching by birefringence, in QPM the effective nonlinearity d_{eff} is reduced by a factor of $2/\pi$ [31].
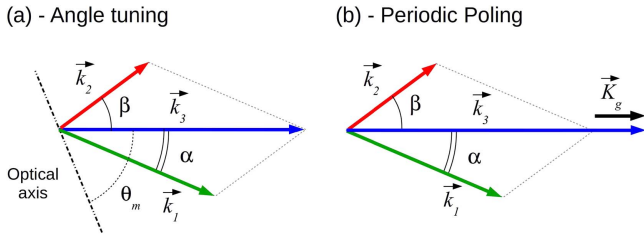
Figure 8. Non-collinear phase-matching configurations for (a) angle-tuned and (b) periodically poled OPAs.

Non-collinear phase matching. When pump, signal and idler beams propagate in different directions, the phase-matching condition becomes the vector equation (2.27). Figure 8(a) shows schematically the k vectors when phase-matching is fulfilled: α and β are the angles between the propagation direction of the pump (k_3) and that of signal (k_1) and idler (k_2), while the direction of the optical axis is taken as the angle θ it forms with the pump beam. Note that in this figure the beams propagate inside the birefringent medium; for the propagation directions outside the crystal, Snell's law must be applied, and therefore the angles become larger. The optical axis must lie on the same plane of the three vectors: according to figure 6, this ensures that only one ordinary and one extraordinary polarisation direction is defined in common to all three beams. As an example, figure 9 sketches the beams of a visible NOPA: the optical axis is on the *horizontal* plane, hence defining the extraordinary polarisation direction and the propagation plane of all beams. Note that propagating the beams along a vertical plane without changing the crystal orientation would dramatically reduce the phase-matching bandwidth. One method to calculate the phase-matching angle θ_m for different values of α is shown in appendix B. Figure 10 shows the signal-wavelength dependent phase-matching angles for visible Type-I NOPAs in BBO, pumped by the SH of a Ti:sapphire ($\lambda = 400$ nm) and an Yb-doped laser ($\lambda = 515$ nm). Similar results in the IR spectral range are shown in 11(a), for a Type-I NOPA in LiIO$_3$, pumped at $\lambda = 800$ nm [32]. In all these curves, the signal/pump angle α is evaluated inside the nonlinear medium.

For the non-collinear geometry, the QPM condition becomes:

$$\Delta\vec{k} = \vec{k}_3 - \vec{k}_2 - \vec{k}_1 - \vec{K}_g, \qquad (2.32)$$

where $\vec{K}_g$ is the grating wave–vector. Figure 8(b) shows the geometric arrangement of the wave–vectors for QPM, for the most common configuration in which the poling is in the direction of the pump beam. Also in the non-collinear case the optical axis forms an angle $\theta = 90°$ with all the wavevectors, so that k_1, k_2 and k_3 can be evaluated independently from the propagation direction. Since in the diagram $|\vec{K}_g|$ is the segment required to close the parallelogram, its calculation is straightforward. Figure 11(b) shows the phase-matching poling period for a NOPA in periodically poled SLT (PPSLT), pumped at $\lambda = 800$ nm and operating in the IR spectral range [32].
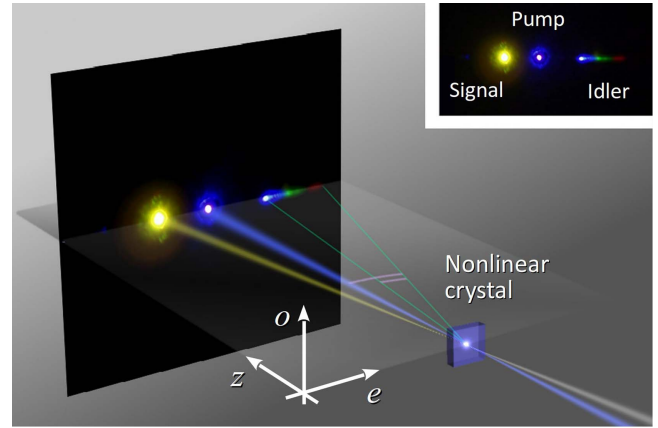

Figure 9. Ordinary and extraordinary directions and propagation plane in a non-collinear OPA.

2.3. Broadband parametric amplification

In section 2.1 we introduced the equations governing parametric amplification of monochromatic waves. In this section we will extend the same concepts to the case of the amplification of ultrashort pulses.

Let's first introduce the coupled nonlinear equations for second order interaction of pulses. Since a pulse is described as (see equation (A.3)):

$$E(z, t) = \frac{1}{2}A(z, t)e^{j(\omega t - kz)} + \text{c.c.,} \qquad (2.33)$$

where $A(z, t)$ is the envelope, then equation (2.4) must be recalculated including time-dependent coefficients $A_i(z, t)$; the resulting coupled nonlinear equations are [36]:

$$\begin{cases} \dfrac{\partial A_1}{\partial z} + \dfrac{1}{2j}\text{GVD}_1\dfrac{\partial^2 A_1}{\partial \tau^2} + \delta_{13}\dfrac{\partial A_1}{\partial \tau} \\ \qquad = -j\sigma_1 A_2{}^* A_3 \cdot e^{-j\Delta kz}, \\ \dfrac{\partial A_2}{\partial z} + \dfrac{1}{2j}\text{GVD}_2\dfrac{\partial^2 A_2}{\partial \tau^2} + \delta_{23}\dfrac{\partial A_2}{\partial \tau} \\ \qquad = -j\sigma_2 A_1{}^* A_3 \cdot e^{-j\Delta kz}, \\ \dfrac{\partial A_3}{\partial z} + \dfrac{1}{2j}\text{GVD}_3\dfrac{\partial^2 A_3}{\partial \tau^2} \\ \qquad = -j\sigma_3 A_1 A_2 \cdot e^{j\Delta kz}, \end{cases} \qquad (2.34)$$

where v_{gi} are the group velocities of the pulses and $\delta_{ij} = 1/v_{gi} - 1/v_{gj}$ is the group velocity mismatch (GVM) between two pulses. Here we have chosen a frame of reference that is moving with the group velocity of the pump pulse ($\tau = t - z/v_{g_3}$); GVD$_i$ are the group-velocity dispersions of the pulses (equation (A.26)), and $\sigma_i = d_{\text{eff}}\omega_i/c_0 n_i$.

Analytically solving these coupled equations, as we did in the previous section, is now more challenging, even in particular cases such as the undepleted-pump regime. To this aim, several numerical methods have been proposed [21, 22] to solve them in particular regimes. However, in order to study the general properties of broadband parametric amplification, a full-blown solution of the coupled equations is not really necessary.
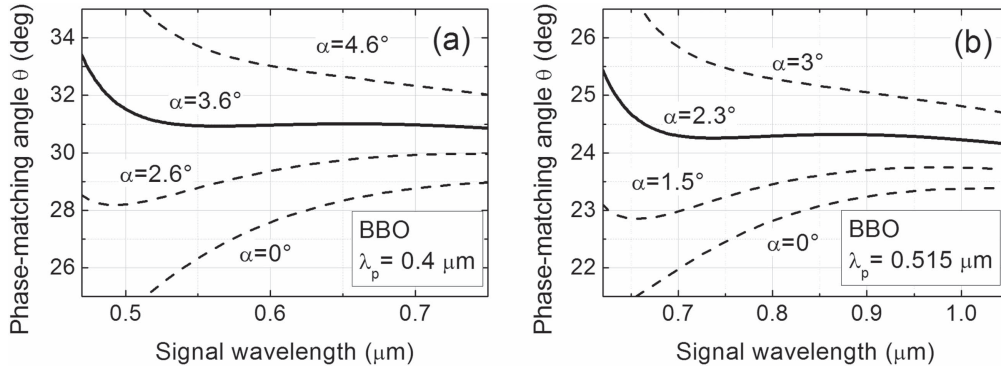
Figure 10. Phase matching for Type-I NOPAs, based on BBO and operating in the visible and near-IR spectral range, for two pump wavelengths. (a) Pump is the second harmonic of a Ti:sapphire laser ($\lambda = 400$ nm) [33–35]; (b) Pump is the second harmonic of a Yb-based laser ($\lambda = 515$ nm). Solid lines are the configurations with the broadest amplification bandwidth. α is signal/pump angle inside the nonlinear medium; $\alpha = 0°$ corresponds to the collinear configuration.
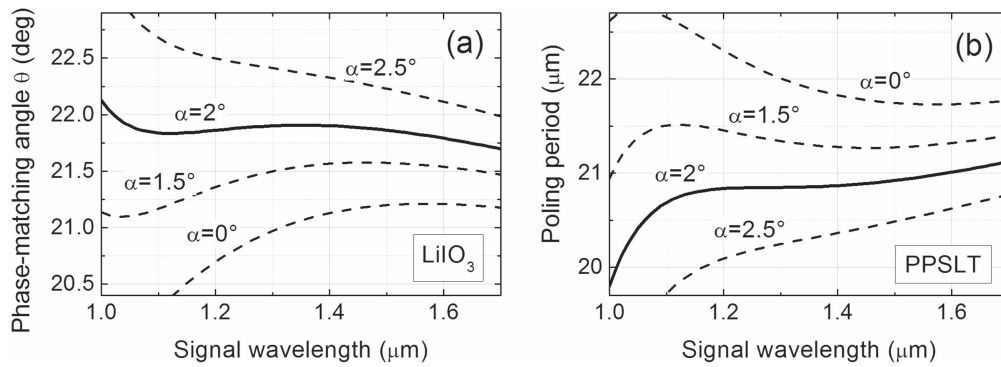

Figure 11. Phase matching for NOPA, pumped by the fundamental of a Ti:sapphire laser ($\lambda = 800$ nm), and operating in the IR spectral range. (a) Phase-matching angles in LiIO$_3$. (b) phase-matching poling period in a periodically poled SLT (PPSLT). Solid lines correspond to the configuration with the broadest amplification bandwidth. α is signal/pump angle inside the nonlinear medium; $\alpha = 0°$ corresponds to the collinear configuration.

As detailed in appendix A.1, a light pulse can be decomposed into the superposition of monochromatic waves by the Fourier transform; and generally, the shorter the pulse, the larger is the number of such waves. Thanks to this feature, many properties of parametric amplification with ultrashort pulses can be deduced by generalising, with suitable corrections, some of the results we derived in the monochromatic regime, such as the parametric gain, the interaction types, the collinear and non-collinear phase-matching.

However, two additional concepts must be introduced to describe an ultrafast OPA: the *pulse-splitting length* and the *phase-matching bandwidth*, that we will discuss in detail in the following paragraphs.

2.3.1. Pulse-splitting length. Although in the monochromatic regime the gain of an OPA scales exponentially with the crystal length, with ultra-short light pulses the optimum crystal length has to be chosen considering also the durations and group velocities of the interacting pulses. One important parameter is the temporal walk-off due to the relative group delay (equation (A.27)) that the pulses accumulate during the propagation. When their relative group delay becomes larger than the pulse-lengths, the pulses do not temporally overlap anymore and their interaction vanishes. Given that the pump

pulse has the FWHM duration τ, one can first calculate the propagation length after which the signal (or the idler) pulse temporally separates from the pump pulse in the absence of gain. This length is called *pulse-splitting length* and depends on the GVM δ between the pulses:

$$ l_{j3} = |\tau/\delta_{j3}| = \left| \tau \left/ \left(\frac{1}{v_{gj}} - \frac{1}{v_{g3}} \right) \right. \right| \qquad j = 1, 2. \quad (2.35) $$

The pulse-splitting length becomes shorter for decreasing pulse duration and for increasing GVM, which depends on the crystal type, pulse wavelengths and (for pulses with extraordinary polarisation) type of phase matching and propagation direction with respect to the optical axis. Note that the GVM between signal/idler and the pump is also contained in equation (2.34).

Once we know the pulse-splitting length, how should we choose the optimal crystal length? There is a qualitatively important difference between the cases in which δ_{13} and δ_{23} have the same or different signs. When $\delta_{13} \cdot \delta_{23} > 0$, both the signal and the idler pulses walk away from the pump in the same direction, so that the amplification process stops for propagation distances longer than the pulse-splitting length and the parametric gain eventually saturates. In this case, the
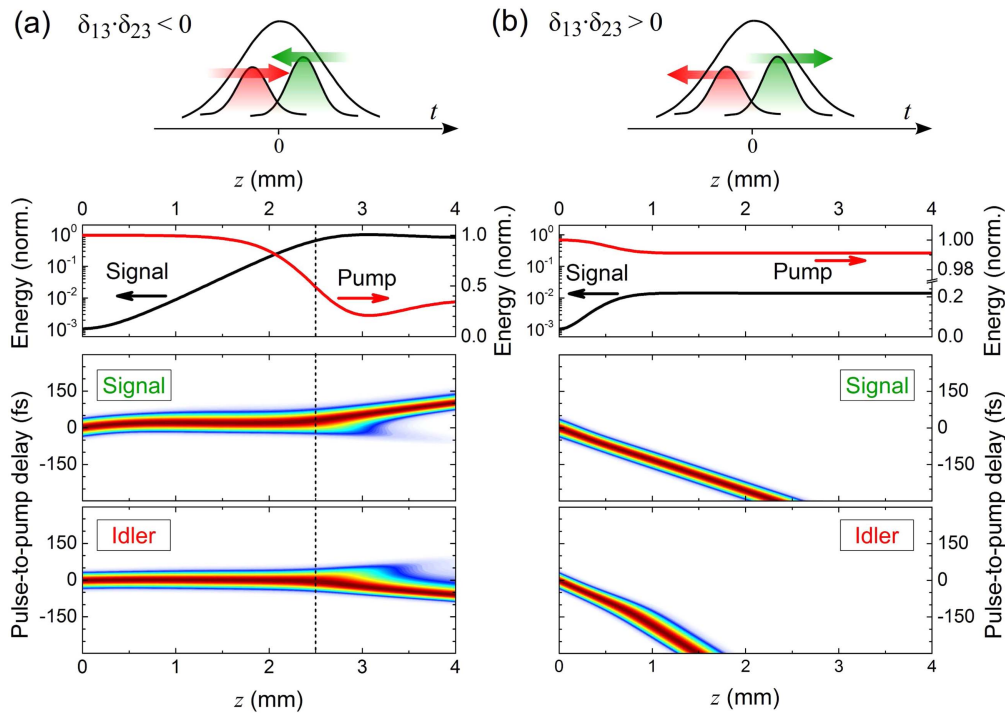
Figure 12. Simulation of signal and idler temporal profiles during amplification for two cases: (a) $\delta_{13} \cdot \delta_{23} < 0$; (b) $\delta_{13} \cdot \delta_{23} > 0$. The reference frame moves with the group velocity of the pump pulse (not shown), which is located at coordinate $t = 0$. Upper panels show the energies of pump (linear scale) and signal pulses (logarithmic scale), lower panels map the normalized pulse intensity as a function of z. Dashed lines in panels (a): crystal coordinate corresponding to pump depletion.

pulse-splitting length represents the length over which parametric interaction takes place, i.e. the maximum useful crystal length: this can be calculated as the smallest value between l_{13} and l_{23}.

On the other hand, when $\delta_{13} \cdot \delta_{23} < 0$ signal and idler pulses walk in opposite direction with respect to the pump; in this way parametric gain can only occur where the leading edge of one pulse and the trailing edge of the other are temporally superposed under the pump pulse. This nonlinear interaction mechanism temporally localises signal and idler under the pump pulse and the gain grows exponentially even for crystal lengths well in excess of the pulse splitting length. To qualitatively understand this trapping effect, we can consider the situation in which the signal pulse has moved slightly to the front and the idler pulse to the back of the pump pulse: during the parametric process, the signal pulse generates idler photons, which move to the back, i.e. towards the peak of the pump; on the other hand, thanks to the feedback mechanism illustrated in figure 3, the idler pulse generates signal photons which in turn move to the front, again towards the peak of the pump. This effect allows to use crystals significantly longer than the pulse-splitting length, and to reach more easily the saturation occurring at pump depletion [37]. This mechanism is illustrated in figure 12, where we show the numerical solution of equation (2.34) for the two different cases. We simulated an OPA employing a 4 mm thick BBO crystal; both pump and signal are 100 fs long. The lower maps show the the normalised temporal intensity of signal and idler during the interaction along the crystal, in a frame of reference moving with the pump,

centered at $t = 0$. The upper panel show the normalised energy of the pump and the signal. panels (a) is for the case in which $\delta_{13} \cdot \delta_{23} < 0$ ($\lambda_1 = 1300$ nm, $\lambda_3 = 800$ nm, Type II (oee), $\delta_{13} = 46.7$ fs mm^{-1}, $\delta_{23} = -23.5$ fs mm^{-1}), and shows that signal and idler remain locked under the pump for propagation lengths much longer than the the pump-signal and pump-idler pulse-splitting length, until pump depletion occurs (dashed line). At depletion, the gain vanishes and the signal and idler become unlocked and travel away from the pump in opposite directions. Panels (b), on the other hand, show that when $\delta_{13} \cdot \delta_{23} > 0$ ($\lambda_1 = 600$ nm, $\lambda_3 = 400$ nm, Type I (ooe) $\delta_{13} = -128.2$ fs mm^{-1}, $\delta_{23} = -238.5$ fs mm^{-1}) signal and idler rapidly move away from the pump in the same direction, limiting the interaction length to only 1 mm; here no pump depletion occurs.

Before concluding this section, we note that to evaluate the pulse-splitting length we only took into account δ_{13} and δ_{23}, accounting for the overlap between the pump and signal/idler pulses. What is the role of δ_{12}, related to the overlap between the signal and the idler pulses? This parameter does not influence the interaction length. However, in the next section we will learn that also δ_{12} plays very important role, though much different: it determines the amplification bandwidth.

2.3.2. Broadband collinear phase-matching. Let us now discuss which parameters determine the gain bandwidth of an OPA. Ideally one would like to have a broadband amplifier, i.e. an amplifier which, for a fixed pump frequency, provides a constant gain over an as broad as possible range

of signal frequencies. As we have deduced in the monochromatic regime both in the undulatory and the corpuscular picture, phase matching is required for the efficient energy flow between the beams. In order to have broadband amplification, one needs to keep the phase mismatch as small as possible over a large bandwidth. Practically, however, the phase-matching condition can be perfectly satisfied only for a given set of frequencies ($\overline{\omega_1}$, $\overline{\omega_2}$, $\overline{\omega_3}$). We will now study in which cases phase-matching is preserved for a broad range of signal frequencies.

In the collinear case, phase mismatch corresponds to:

$$\Delta k = k(\omega_3) - k(\omega_2) - k(\omega_1) \tag{2.36}$$

for the birefringent phase-matching and

$$\Delta k = k(\omega_3) - k(\omega_2) - k(\omega_1) - K_g \tag{2.37}$$

for QPM. Let us first evaluate how the phase mismatch changes when the signal frequency is detuned from $\overline{\omega_1}$, which corresponds to the phase-matching angle $\overline{\theta_m}$. One direct way is to numerically calculate Δk as a function of the signal frequency, and then evaluate the gain from equations (2.12) and (2.13), within the large gain and low pump-depletion approximations. This approach has the great advantage of providing the frequency-dependent OPA gain, from which it is possible to obtain the spectrum of the amplified signal, and to evaluate the corresponding TL duration. We will give details and examples of this procedure later in section 2.3.4.

Another approach consists in the first-order Taylor expansion of Δk (equations (2.26) or (2.31)) as follows. If the pump frequency is fixed at $\overline{\omega_3}$ and the signal frequency changes to $\overline{\omega_1} + \Delta\omega$, then by energy conservation the idler frequency changes to $\overline{\omega_2} - \Delta\omega$. The corresponding wave vectors become, to the first order:

$$k(\overline{\omega_1} + \Delta\omega) \simeq k(\overline{\omega_1}) + \left.\frac{\partial k_1}{\partial\omega}\right|_{\omega_1} \times \Delta\omega$$

$$= k(\overline{\omega_1}) + \frac{1}{v_{g1}}\Delta\omega$$

$$k(\overline{\omega_2} - \Delta\omega) \simeq k(\overline{\omega_2}) - \left.\frac{\partial k_2}{\partial\omega}\right|_{\omega_2} \times \Delta\omega$$

$$= k(\overline{\omega_2}) - \frac{1}{v_{g2}}\Delta\omega, \tag{2.38}$$

where v_{g1} and v_{g2} are the group velocities of signal and idler pulses, respectively evaluated at frequencies $\overline{\omega_1}$ and $\overline{\omega_2}$. The resulting wave–vector mismatch is:

$$\Delta k \simeq \left(\frac{1}{v_{g_1}} - \frac{1}{v_{g_2}}\right)\Delta\omega = \delta_{12}\Delta\omega, \tag{2.39}$$

where δ_{12} is the GVM between signal and idler pulses, calculated at phase matching. This equation states that the slope of the wave–vector mismatch as a function of frequency is δ_{12}, and that the broadest phase-matching condition is fulfilled when $\delta_{12} = 0$, that is when signal and idler propagate with matched group velocities. Note that this result holds for both the birefringent and QPM configurations, since K_g is constant and vanishes upon differentiation. The approach
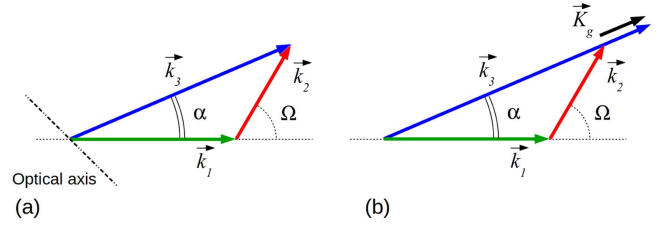

Figure 13. Geometrical arrangement of signal, pump and idler wave–vectors for the calculation of the broadband non-collinear condition, for birefringent (a) and QPM (b) phase matching.

based on Taylor expansion, although limited to the first order, provides a prescription on the signal/idler GVM for the design of a broadband collinear OPA. If we now insert the Taylor expansion of Δk into equations (2.12) and (2.13), we can obtain an approximate expression of the FWHM parametric gain bandwidth, within the large gain and low pump-depletion approximation, as:

$$\Delta\nu = \frac{2\sqrt{\ln 2}}{\pi}\sqrt{\frac{\Gamma}{L}}\frac{1}{|1/v_{g_2} - 1/v_{g_1}|}. \tag{2.40}$$

This equation shows that the gain bandwidth is inversely proportional to the GVM between signal and idler and has only a weaker square root dependence on small-signal gain and crystal length. For the case when $v_{g_1} = v_{g_2}$, equation (2.40) loses validity and equation (2.38) must be expanded to the second order, giving:

$$\Delta\nu = \frac{2\sqrt[4]{\ln 2}}{\pi}\sqrt[4]{\frac{\Gamma}{L}}\frac{1}{\sqrt{|\mathrm{GVD}_1 + \mathrm{GVD}_2|}}. \tag{2.41}$$

In this case the gain bandwidth is inversely proportional to the square root of the sum of the GVDs of signal and idler pulses.

Group-velocity matching is typically fulfilled for Type-I phase-matching at degeneracy, that is when signal and idler have the same frequency and polarisation, and hence the same group velocity. For a pump at angular frequency $\overline{\omega_3}$, this occurs when $\overline{\omega_1} = \overline{\omega_2} = \overline{\omega_3}/2$.

2.3.3. Broadband non-collinear phase matching. The same calculations can be performed for the non-collinear case, taking into account the vectorial nature of the phase matching condition. Here we will expand to the first order:

$$\Delta\vec{k} = \vec{k}(\omega_3) - \vec{k}(\omega_2) - \vec{k}(\omega_1) \tag{2.42}$$

for the birefringent phase-matching (figure 13(a)) and

$$\Delta\vec{k} = \vec{k}(\omega_3) - \vec{k}(\omega_2) - \vec{k}(\omega_1) - \vec{K_g} \tag{2.43}$$

for QPM (figure 13(b)). The expansion is performed around ($\overline{\omega_1}$, $\overline{\omega_2}$, $\overline{\omega_3}$), where $\Delta\vec{k} = 0$, which corresponds to:

$$\begin{cases} \overline{k_3}\cos\alpha = \overline{k_1} + \overline{k_2}\cos\Omega & \text{parallel to signal,} \\ \overline{k_3}\sin\alpha = \overline{k_2}\sin\Omega & \text{normal to signal.} \end{cases} \tag{2.44}$$

Note that according to the second equation the idler is angularly dispersed, since Ω depends on k_2.
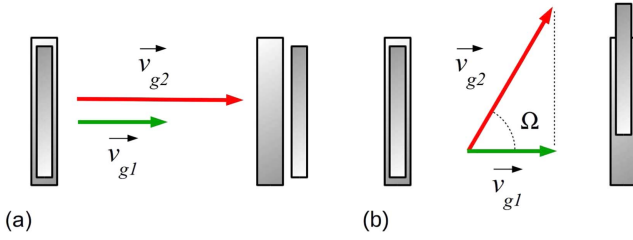
Figure 14. Sketch of signal and idler pulses during propagation in the gain medium. (a) Narrowband collinear configuration corresponds to temporal walk-off of the pulses. (b) The angle Ω required for broadband amplification also leads to exact signal-idler temporal overlap.

Let's now evaluate $\Delta \vec{k}$ when the signal is detuned by $\Delta \omega$; in this case the detuned wave–vectors become $\vec{k_1} = \vec{\bar{k}_1} + \Delta \vec{k_1}$ and $\vec{k_2} = \vec{\bar{k}_2} + \Delta \vec{k_2}$. The projection of the wave–vector mismatches on the directions parallel ($\parallel$) and perpendicular ($\perp$) to the signal gives, for both cases of figure 13:

$$\begin{cases} \Delta k_\parallel = -\Delta k_{2\parallel} - \Delta k_{1\parallel}, \\ \Delta k_\perp = -\Delta k_{2\perp} - \Delta k_{1\perp}. \end{cases} \quad (2.45)$$

By expanding $\Delta \vec{k_1}$ and $\Delta \vec{k_2}$ to the first order and imposing $\Delta k_\parallel = 0$ and $\Delta k_\perp = 0$, we get:

$$\begin{cases} \Delta k_\parallel = \left.\dfrac{\partial k}{\partial \omega}\right|_{\omega_2} \cos \Omega \cdot \Delta \omega - k_2 \left.\dfrac{\partial \Omega}{\partial \omega}\right|_{\omega_2} \\ \qquad\quad \times \sin \Omega \cdot \Delta \omega - \left.\dfrac{\partial k}{\partial \omega}\right|_{\omega_1} \Delta \omega = 0, \\ \Delta k_\perp = \left.\dfrac{\partial k}{\partial \omega}\right|_{\omega_2} \sin \Omega \cdot \Delta \omega + k_2 \left.\dfrac{\partial \Omega}{\partial \omega}\right|_{\omega_2} \\ \qquad\quad \times \cos \Omega \cdot \Delta \omega = 0. \end{cases} \quad (2.46)$$

By further mathematical manipulation, we obtain the simple expression:

$$v_{g1} = v_{g2} \cos \Omega \quad (2.47)$$

which shows that, as in the collinear case, broadband amplification is obtained when the group-velocity of the signal matches the projection of the group velocity of the idler along the signal direction (see figure 14). Equation (2.47) can be satisfied only if $v_{g2} > v_{g1}$. Note that in the case of

periodically poled crystals, this equation involves the group velocities of the bulk material, since the poling wavevector vanishes upon differentiation.

2.3.4. Amplification bandwidth. In this section we examine the OPA configurations for broadband amplification. The expansion-based method we have illustrated in sections 2.3.2 and 2.3.3, helps at a first stage to sort the configurations and the crystals leading to broad amplification bandwidth. Figure 15 plots the GVM δ_{12} between signal and idler, as a function of signal wavelength for several nonlinear optical crystals and spectral ranges, using Type I phase matching. As expected, in all cases group velocity matching is obtained at the degeneracy point (800 nm when $\lambda_3 = 400$ nm, and 1.6 μm when $\lambda_3 = 800$ nm), where signal and idler share the same wavelength and polarisation. At these wavelengths, broadband amplification is achieved with collinear geometry.

Other configurations with potentially broad amplification bandwidths are those with $\delta_{12} > 0$: in this case, $v_{g2} > v_{g1}$, i.e. the idler has higher group velocity than the signal, which can thus be projected along the signal direction to achieve the group velocity matching expressed by equation (2.47). For BBO (solid curve) $\delta_{12} < 0$ for all signal wavelengths in the IR. This can be understood by recalling that BBO is a relatively low-refractive-index material ($n = 1.6$) with a zero-dispersion wavelength at 1.38 μm. Since the zero-dispersion wavelength corresponds to a maximum of the group velocity, the signal wavelength is in a region of high group velocity, and the idler is necessarily slower. For crystals with higher refractive indexes the zero-dispersion wavelength shifts to longer wavelengths (for example, 1.92 μm in LiNbO$_3$, which has $n = 2.2$), so that the idler can be expected to move faster than the signal. For these crystals, therefore, the group velocities of the signal and idler can be matched in a non-collinear interaction geometry, which can be potentially exploited for broadband amplification.

After selecting the crystals that have $\delta_{12} > 0$ in the amplification band, it is possible to calculate the angle α providing the broadest the gain bandwidth. To this aim, we can follow two approaches:
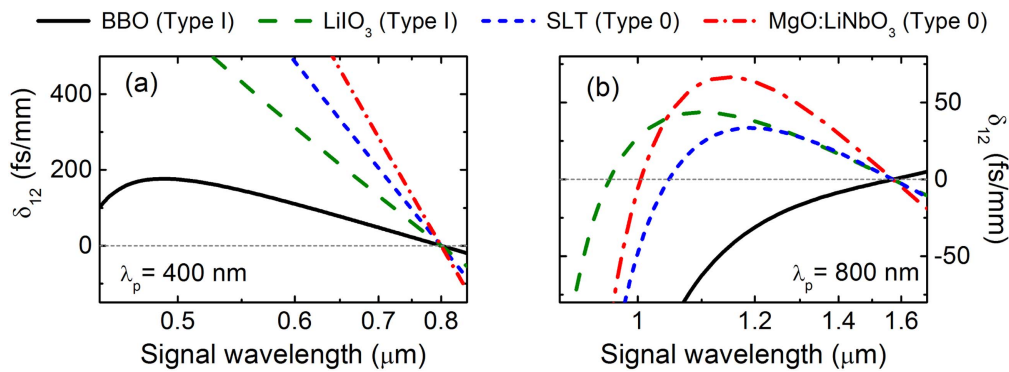

Figure 15. Calculated signal-idler group-velocity mismatch for several nonlinear optical crystals. (a) At 400 nm pump wavelength in the visible; (b) at 800 nm pump wavelength in the near-IR. Data from [32].
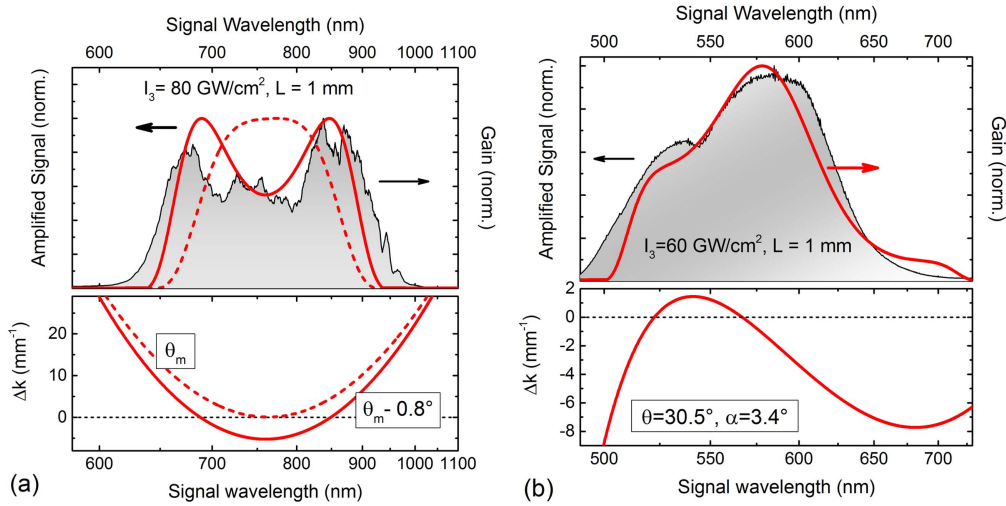
Figure 16. Gain of 390-nm-pumped OPAs, compared with the measured spectra. The gain medium is a 1 mm thick BBO. Lower panels: calculated wave–vector mismatch; main panels: corresponding normalized gain (red lines) and experimental spectrum (black line). (a) Collinear OPA around degeneracy; dashed line: BBO tuned exactly at degeneracy angle $\theta_m = 30.7°$; solid line: BBO detuned to broaden the gain bandwidth. (b) NOPA. The gain includes the transmission of a short-pass filter on the seed beam.
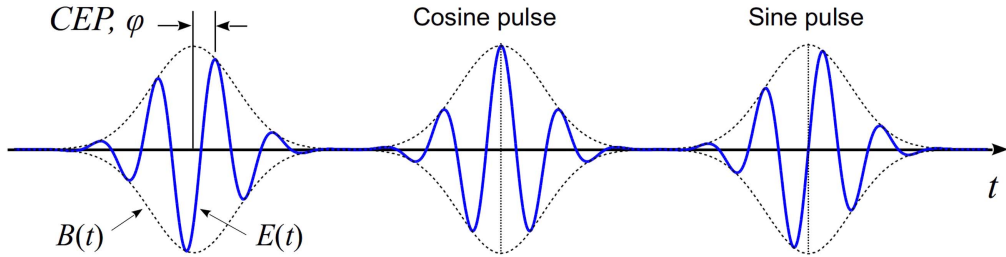

Figure 17. Definition of the CEP slip, a cosine pulse ($\varphi = 0$) and sine pulse ($\varphi = \pi/2$).

- We calculate the phase-matching curves, as the ones shown in figures 10 and 11; the angle α for which the curve is nearly independent from the signal wavelength corresponds to an ultrabroadband amplifier. In our examples, the broadband configuration is indicated in solid line.

- Even better estimate of the amplification bandwidth can be obtained by calculating the frequency-dependent gain. The approach is similar for angle- and poling-period-tuning: from those curves of figures 10 and 11 corresponding to the optimal angle α, we find θ_m or Λ_m. Then we calculate the frequency-dependent wavevector mismatch $|\Delta \vec{k}(\omega)|$ (see appendix B for details). Finally, the frequency-dependent gain is calculated by substituting $|\Delta \vec{k}(\omega)|$ in equations (2.12) and (2.13).

This last method gives the best estimation of the OPA gain bandwidth, because it also takes into account the crystal thickness, the pump intensity and the exact wavelength-dependent wave–vector mismatch. It provides the most reliable approximation of the gain spectrum and allows further optimisation the amplification bandwidth by exploring several values of α. Figure 16 shows the calculated wave–vector mismatch and expected gain bandwidth evaluated thanks to this approach, at various configurations. Note that in

the case of degenerate OPA, shown in panel (a), this method allows to evaluate the gain bandwidth also when the crystal is detuned (solid line) from perfect phase matching (dashed line) so as to obtain $\Delta k = 0$ at multiple signal wavelengths and in this way broaden the gain bandwidth.

2.4. The idler beam

So far we have focused on the signal beam of an OPA, however also the idler can be used for several applications. The most important ones are the passive CEP stabilisation, and the extension of the OPA tunability to the IR spectral range. Let us first study the unique properties of the idler for passive CEP stabilisation.

We will consider a pulse with electric field $E(t) = B(t)\cos(\omega_0 t + \phi)$, where ϕ is the (time-dependent) phase. $\varphi = \phi(t = 0)$ is the CEP, otherwise referred to as absolute phase: when the pulse envelope $B(t)$ has its maximum at $t = 0$, φ is the phase of the carrier wave with respect to the envelope, as shown in figure 17. If $\varphi = 0$, a maximum of the electric field corresponds to the peak of the pulse envelope (cosine pulse), while if $\varphi = \pi/2$, the electric field at the peak of the pulse envelope is zero (sine pulse). Typical femtosecond laser sources generate pulse trains in which the CEP varies from pulse to pulse [38]. One of the frontiers of

ultrafast optics is the stabilisation of the CEP, which allows the generation of light pulses with predetermined and reproducible electric field profile. This capability, acquired only in recent years [39, 40], has paved the way to the synthesis of optical waveforms [41], analogously to the electrical waveforms produced by an electronic pulse generator. CEP control, in particular, is a prerequisite for strong-field physics with ultrashort pulses and has allowed the production of isolated attosecond pulses through high harmonic generation [42, 43].

To understand how the OPA can contribute to the stabilisation the idler CEP, we need to derive a link between the CEPs of pump, signal and idler waves. In particular, since the CEP is related to the shift of the carrier with respect to the envelope, we will focus on the three-wave mixing of monochromatic waves, for which A_i and ϕ do not depend on time. In this case the CEP is $\varphi \equiv \phi$, and the nonlinear interaction is described by the coupled equation (2.8). Recalling that the complex field amplitudes A_i depend on the real amplitudes B_i as (see appendix A.1)

$$A_i = B_i e^{j\varphi} \tag{2.48}$$

the coupled nonlinear equations are transformed to [24]:

$$\begin{cases} \dfrac{\partial B_1}{\partial z} = \sigma_1 B_2 B_3 \sin \Psi, \\[2mm] \dfrac{\partial B_2}{\partial z} = \sigma_2 B_1 B_3 \sin \Psi, \\[2mm] \dfrac{\partial B_3}{\partial z} = -\sigma_3 B_1 B_2 \sin \Psi, \\[2mm] \dfrac{\partial \Psi}{\partial z} = \left(\sigma_1 \dfrac{B_2 B_3}{B_1} + \sigma_2 \dfrac{B_1 B_3}{B_2} - \sigma_3 \dfrac{B_1 B_2}{B_3} \right) \cos \Psi - \Delta k, \end{cases}$$

$$\tag{2.49}$$

where $\Psi = \varphi_3 - \varphi_2 - \varphi_1 - \Delta kz$ is the so-called generalised phase. Assuming perfect phase matching ($\Delta k = 0$) equation (2.49) have simple solutions for different boundary conditions.

Let us first consider the case of SFG, i.e. the generation of a field at $\omega_3 = \omega_1 + \omega_2$; assuming the boundary condition $B_3(z = 0) = 0$, the value of the generalised phase that maximises the right-hand side in the third equation in (2.49) is $\Psi = -\pi/2$. This corresponds to the SFG phase $\varphi_{\mathrm{SFG}} = \varphi_3 = \varphi_1 + \varphi_2 - \pi/2$. With SHG, which is a degenerate SFG process with $\omega_1 = \omega_2 = \omega_{\mathrm{FF}}$ and $\omega_3 = \omega_{\mathrm{SH}} = 2\omega_{\mathrm{FF}}$, we get $\varphi_{\mathrm{SH}} = 2\varphi_{\mathrm{FF}} - \pi/2$.

In an OPA, the idler pulse (ω_2) is generated through a DFG process between pump (ω_3) and signal (ω_1), i.e., $\omega_2 = \omega_3 - \omega_1$: assuming the boundary condition $B_2(z = 0) = 0$, the value of the generalised phase that maximises the right-hand side term in the second equation in (2.49) is $\Psi = \pi/2$. Consequently, $\varphi_{\mathrm{DFG}} = \varphi_2 = \varphi_3 - \varphi_1 - \pi/2$, which inherently links the CEP of the idler to those of the signal and the pump. Hence, if φ_3 and φ_1 are relatively fixed (i.e., up to an arbitrary constant), then the DFG phase is constant from pulse to pulse.

This process can be used to obtain a train of pulses with constant CEP starting from pulsed laser sources where the

CEP φ varies randomly from shot to shot. This technique is called *passive CEP stabilisation* [44], and will be detailed in the following.

Let us consider an OPA in which the seed pulse is obtained by self-phase-modulation (SPM) starting from a driver pulse with CEP φ. This is for example the case of spectral broadening in a single-mode or microstructured optical fiber, in a gas-filled hollow waveguide or a gas filaments, or of white-light continuum (WLC) generation in bulk materials (see section 3.2). In all these cases, it can be shown [45] that $\varphi_{\mathrm{SPM}} = \varphi - \pi/2 + c$, i.e. the CEP of the driver pulse is transferred to the seed. Here and in the following, we include also the *constant* phase c accumulated due to propagation.

When the OPA is pumped by the FF of the laser, $\varphi_3 = \varphi + c_3$; if the seed pulse is produced via WLC generation starting from the FF pulse, then its CEP is linked to that of the pump by $\varphi_1 = \varphi - \pi/2 + c_1$ and the idler has CEP $\varphi_2 = \varphi_3 - \varphi_1 - \pi/2 = c_3 - c_1$, which is stable from shot to shot. The same situation holds when the OPA is pumped by the SH of the driving pulse, so that $\varphi_3 = 2\varphi - \pi/2 + c_3$; if the WLC seed is also generated starting from the SH of the driver, then $\varphi_1 = 2\varphi - \pi + c_1$ and $\varphi_2 = c_3 - c_1$, resulting again in passive CEP stabilisation of the idler. We can thus conclude that an OPA produces a CEP stable idler when the seed is generated with the same pulse used as the pump, either the FF or the SH of the driving laser. If, on the other hand, the OPA is pumped by the SH but the seed is generated starting from the FF, we have $\varphi_3 = 2\varphi - \pi/2 + c_3$ and $\varphi_1 = \varphi - \pi/2 + c_1$. In this case, we obtain $\varphi_2 = \varphi - \pi/2 + c_3 - c_1$, so that the idler is not CEP stabilised, but rather reproduces, from shot to shot, the CEP fluctuations of the driving pulse (phase-repeating OPA) [46].

The above considerations are valid when the OPA is seeded by WLC, which inherits the CEP of the driving pulse. For parametric superfluorescence (PSF), which is parametric amplification of vacuum fluctuations or quantum noise (see section 3.2), one expects that the CEP link between the pump and the PSF pulses is completely lost; this has indeed been verified, both numerically and experimentally, in [22]. CEP locking between the pump and PSF pulses only holds at degeneracy [47, 48]. Therefore, in most cases, an OPA seeded by PSF cannot be used in any passive CEP stabilisation scheme. It should be noted that, for a multistage OPA driven by a sufficiently intense pump, efficient amplification of PSF with random CEP takes place even in the absence of a seed beam. This mechanism can compete with the amplification of the WLC seed causing extra CEP jitter and even excessive amplitude noise. Therefore, to suppress the parasitic amplification of PSF, the pump intensity and the gain of each OPA stage should be carefully optimised [49].

Another important application of the idler beam is direct generation of tunable mid-infrared radiation. If we consider the bandwidth $\Delta\omega_3$ of the pump beam to be sufficiently narrow, one can easily derive from energy conservation that $|\Delta\omega_2| = |\Delta\omega_1|$, i.e. the idler inherits the bandwidth of the amplified signal. The idler propagates along directions imposed
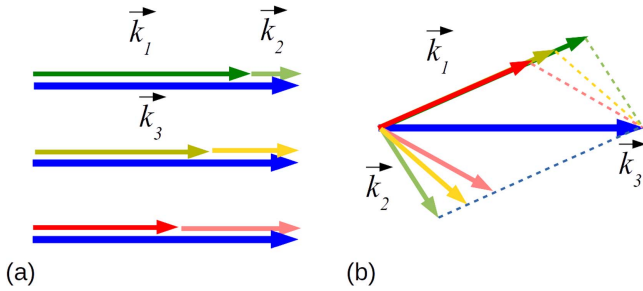
Figure 18. Propagation direction of the beams in the collinear (a) and non-collinear (b) cases. The direction of the idler wavevector $\vec{k}_2$ is deduced from phase-matching considerations.

by the phase-matching condition, which in its vector notation reads $\vec{k}_3 = \vec{k}_1 + \vec{k}_2$ (see figure 18). In collinear OPAs, $\vec{k}_3$ and $\vec{k}_1$ are parallel, and the idler is also generated collinearly with pump and signal (panel (a)). On the other hand, in NOPAs $\vec{k}_3$ and $\vec{k}_1$ form a finite angle and the idler is also generated in a non-collinear direction. As illustrated in figure 18(b), a broadband NOPA produces angularly dispersed idler pulses, which are very difficult to be practically employed. Grating and prism-based systems could be used to correct for the angular dispersion of the idler beam [46],but at the price of a significant complication of the experimental setup. However, another approach is feasible for the non-collinear generation idler pulses without angular dispersion. Thanks to the symmetry between signal and idler (see equations (2.8) and (2.34)), we could call A_1 the idler and A_2 the signal. In this case, figure 18(b) suggests that the idler beam (see $\vec{k}_1$) can be generated without angular dispersion if the input seed (see $\vec{k}_2$) has suitable angular dispersion [50]. The non-collinear phase-matching still obeys equation (2.47), which now means that broadband idler pulses are obtained when the group-velocity of the idler matches the projection of the group velocity of the signal along the idler direction. This can be satisfied only if the group velocity of the signal is higher than that of the idler.

3. Design criteria of ultrafast OPAs

In this section we will discuss the design criteria of ultrafast OPAs. The way an OPA is implemented depends on its architecture, the characteristics of the laser source, the amplification frequency range, the amplified pulse energy and duration.

3.1. OPA architecture

The conceptual scheme of a femtosecond OPA is summarised in figure 19. One can see that an OPA fundamentally consists of three sub-systems [51]:

(a) A seed pulse generation stage, which exploits a nonlinear optical process to generate, starting from the pump pulse, from its second harmonic (SH) or from its third harmonic (TH), a weak pulse at the signal frequency that initiates the OPA process.

(b) Parametric amplification in one or more gain stages, pumped either by the fundamental wavelength (FW) of the driving laser or by its SH/TH.

(c) An optional pulse compression stage by a dispersive delay line, to obtain the TL pulse duration.

Analyzing the operation of these three blocks provides the key for understanding the properties of the OPA and in particular the design required to achieve specific working parameters. Typically gain in an OPA is achieved in multiple stages, with the number dictated by the final pulse energy: a pre-amplifier (or signal amplifier, 1st stage) starting from the low-energy seed beam and displaying high gain (from 10^3 to 10^5) and one (2nd stage) or more power amplifiers, displaying relatively low gain (from 10 to 10^2). The multi-stage approach has several advantages: (i) it allows to compensate for the GVM arising between pump and signal pulses within each stage; (ii) it enables to adjust the pump intensity, and thus the parametric gain, separately in the different stages. Most of the available pump energy should be used for the final stage, which is driven into saturation in order to efficiently convert the available pump energy and minimise shot-to-shot energy fluctuations of the amplified signal. The spot size of the beams progressively increases for the subsequent stages, in order to accommodate higher pulse energies while keeping comparable peak intensities.
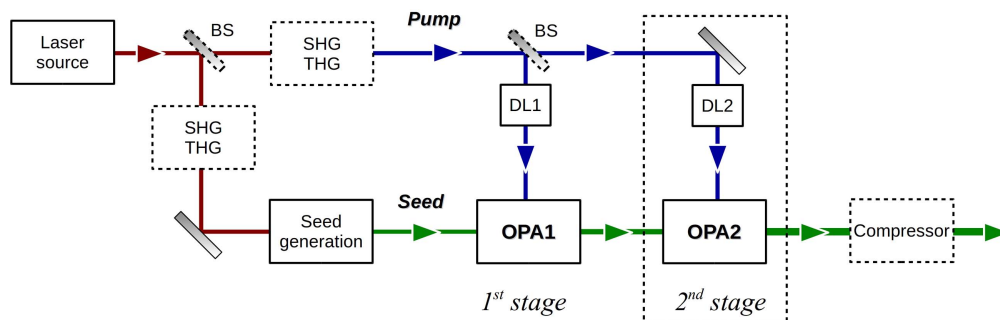

Figure 19. Conceptual scheme of a femtosecond OPA. DL: delay line; BS: beam splitter; SHG/THG: second/third-harmonic generation module. Dashed boxes denote optional stages.
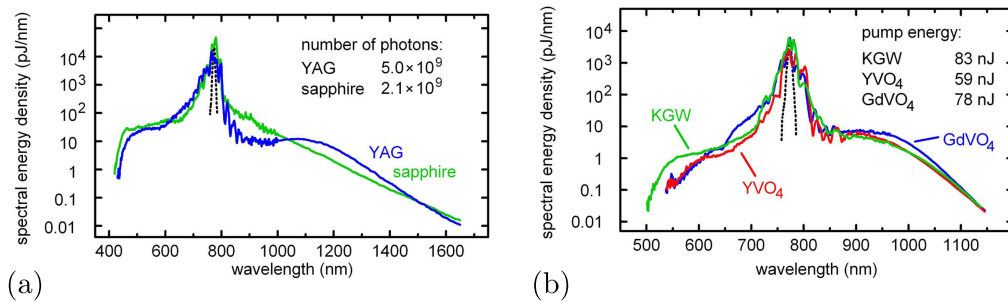
Figure 20. White light spectra generated by 775 nm pulses (dotted black lines, not in scale) in several transparent plates: (a) yttrium aluminum garnet (YAG) and sapphire; (b) potassium–gadolinium tungstate (KGW), yttrium vanadate (YVO_4) and gadolinium vanadate ($GdVO_4$). All plates are 4-mm-thick, except for sapphire, which has thickness of 3 mm. Data from [59].

3.2. Seed generation

In standard OPA systems, the two most widely adopted schemes for producing the seed pulse are optical parametric generation (OPG) and WLC generation. OPG, also known as PSF, is parametric amplification of the vacuum or quantum noise, which can also be thought of as two-photon spontaneous emission from a virtual level excited by the pump field [52]. In practice it is simply achieved by pumping a suitable second order nonlinear crystal, which is often of the same Type as the ones used in the subsequent OPA stages; OPG occurs at those frequencies for which the parametric interaction is phase-matched. Since PSF is a stochastic process that starts from noise, it has the disadvantages of a inherently large shot-to-shot energy fluctuations of the seed and a poor spatial beam quality. In addition, the longitudinal position inside the nonlinear crystal at which amplification takes place, and thus the absolute timing of the seed pulse with respect to the pump, varies stochastically in time [22]. Finally, the CEP of the seed generated by OPG is completely uncorrelated to the CEP of the pump pulse, so that passive CEP stabilisation schemes cannot be applied to OPAs seeded by OPG [22] (see section 2.4). The main advantage of OPG is the relatively modest pulse energy requirement, especially using crystals with very high effective nonlinearity such as periodically poled LN and SLT. This features is particularly useful in OPAs which are driven by high-repetition-rate, low-pulse-energy oscillators [53, 54]. One final remark about OPG is that it often occurs as a parasitic effect, as it can be generated in the initial stage(s) of the OPA, in the absence of a proper seed, and then amplified in the subsequent stages, thus spoiling the properties (energy stability, spectral purity, CEP stability) of the amplified pulses. This problem is especially relevant for the OPCPAs, in which there might be temporal windows of the relatively long pump pulse which are not seeded. Therefore, special care needs to be taken to design the OPA stages in order to suppress OPG/PSF [55, 56]. WLC generation [57] is achieved by focusing the femtosecond pulse in a suitable transparent dielectric medium (typically a sapphire plate) displaying a $\chi^{(3)}$ nonlinearity. It is a complicated nonlinear optical process, involving the interplay and coupling of temporal (self-phase modulation, dispersion, self-steepening) and spatial (self-focusing, diffraction) aspects, as well as ionisation and plasma generation [58] leading to the

formation of a filament and to dramatic spectral broadening. WLC generation is performed by focusing a fraction of the driving pulse (typically the FF off the laser, but sometimes also the SH or the TH) into the plate (with thickness from 1 to 10 mm); by adjusting the pulse energy (using a variable attenuator), the focusing conditions (by moving the plate in the focus of the beam) and the numerical aperture of the focused beam (often by a diaphragm placed in front of the focusing lens) a single filament WLC is formed. Typical WLC spectra are shown in figure 20 [59]: besides an intense residual peak at the driving pulse wavelength (which actually contains most of the energy), two broad continua are formed to the blue and to the red, with spectral energy density which is 3 and 4 orders or magnitude lower than that of the driving pulse, and amounts to $\simeq 10–30$ pJ nm^{-1} in the visible range. The WLC displays excellent shot-to-shot stability and diffraction-limited spatial beam quality, so that it is the ideal seed for an OPA [60] although with limited spectral energy density. Using 800 nm Ti:sapphire driving lasers, with pulse duration of 100 fs or shorter, the best medium for WLC generation is undoped sapphire which, due to its very high thermal conductivity and damage threshold, guarantees excellent stability and damage-free operation. Using plates with 1–3 mm thickness and pulse energies of $\simeq 1$ μJ, the WLC spectrum extends down to 0.45 μm in the visible and up to 1.6 μm in the IR [61]. The spectral coverage of WLC can be extended to the UV ($\simeq 340$ with FF pump and 250 nm with SH pump) using CaF_2, which needs to be continuously moved in the focal plane to avoid photodamage [62]. CaF_2 is however seldom used in combination with OPAs, as the UV range is very difficult to amplify (as discussed in section 3.3.1). Using 1030 nm Yb-based driving lasers, which generate longer pulses, sapphire is not a suitable material for WLC generation. Other media with lower bandgap, such as undoped YAG or undoped KGW, allow the generation of stable WLC under these conditions [59, 63]. In particular, for the 200–400 fs pulses typically generated by Yb:based systems, a 4–6 mm thick YAG plate allows the damage-free generation of a stable WLC [64]. The WLC generated in sapphire/YAG provides a very broadband seed; the duration of the OPA pulses will depend on the fraction of this broad bandwidth which can be amplified, i.e. on the gain bandwidth of the OPA crystal(s), which has been discussed in
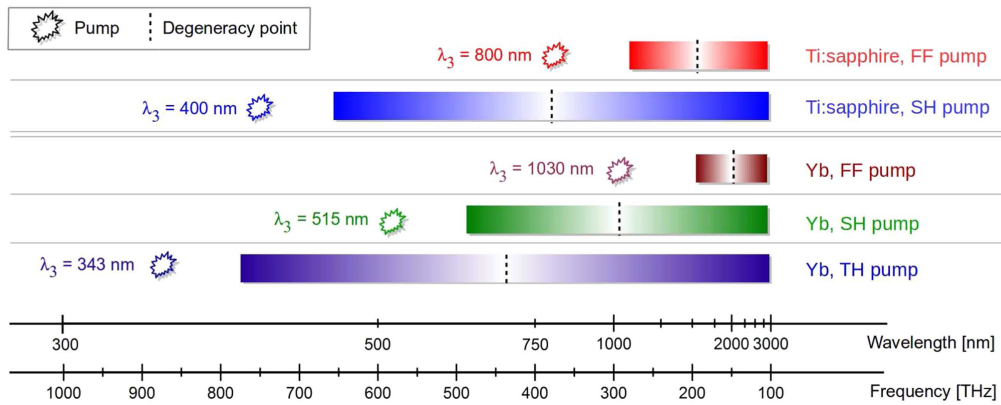
Figure 21. Map of tuning ranges of an OPA based on BBO, whose infrared transparency is limited to 3 μm. The degeneracy point is at half the pump frequency.

section 2.3. One can thus derive the following design rules for the OPA seed generation:

D1 Whenever possible, use WLC as a seed for the OPA, due to the superior temporal and spatial qualities and the very high shot to shot stability.

D2 OPG can be employed if the pulse energy available to drive the seed generation is too low, as in high-repetition-rate, low-energy systems; care should be taken to avoid OPG as a parasitic effect which can occur in the different OPA stages, providing a spurious seed which degrades the quality of the amplified pulses.

D3 Sapphire is the preferred option as a WLC material, due to its high stability and damage threshold; for longer driving pulses, such as those generated by Yb-based systems, low-bandgap materials such as YAG are better options.

3.3. Parametric amplification

In the parametric amplification stage(s) energy flows from the pump to the seed pulses. In order to optimise this process, one should carefully adjust the pump-pulse (wavelength, energy and duration) and the nonlinear interaction (crystal Type and crystal length) parameters.

3.3.1. Pump-pulse parameters.
Among the most important parameters which influence the performances of an OPA are the characteristics of the pump pulse, and in particular: its wavelength, which determines the tuning range; the pulse energy and duration, which affects the interaction length, the gain and the maximum energy of the amplified signal; the repetition rate, which determines the average power flowing through the crystal(s).

Pump-pulse wavelength. Several criteria influence the choice of the pump wavelength for an OPA. The most important is the required tuning range, which depends on the pump wavelength, on the possibility to satisfy the phase-matching condition and on the transparency range of the nonlinear crystal. Absorption is one of the most important factors limiting the tuning of an OPA; care must be taken in

order to have both signal and idler frequencies in the transparency range of the nonlinear crystal(s). This is due to the feedback mechanism we described in section 2.1: not only does it guarantee the exponential growth of the gain, but it also prevents amplification whenever a signal or idler photon is absorbed. For this reason, absorption of the idler light in the infrared affects the amplification in the visible. In figure 21 we summarise the tuning ranges of the popular BBO-based OPA, when pumped by the FF and the SH of Ti:sapphire and by the FF/SH/TH of Yb. For this crystal and these pumping conditions wavelength tunability is between 390 nm and $\approx$3 μm, limited by the pump pulse wavelength and by the onset of IR absorption in BBO at $\approx$3 μm. Of course other frequency ranges can be covered by nonlinear frequency conversion of the OPA output, e.g by SHG of or by SFG with the FF or the SH of the driving pulses. In particular, the mid-IR region (3–20 μm), which is very important for vibrational spectroscopy, can be covered by DFG between the signal and the idler of a 800 nm pumped OPA [65, 66]. By inspecting figure 21, one notices that for FF-pumped OPAs signal/idler tunability is limited to the IR. By frequency doubling an FF-pumped OPA, one can only generate signal wavelengths down to 550 nm, thus leaving a significant portion of the visible uncovered. The visible region (450–700 nm), which is very important for spectroscopic applications, can be well covered by a SH-pumped Ti:sapphire OPA; on the other hand, for Yb lasers a visible OPA requires pumping with the TH, with an additional frequency conversion process which reduces the overall conversion efficiency.

The tuning range of OPAs in the visible is limited to $\simeq$390 nm (when pumped by the TH of an Yb laser) by the energy of the pump photon; pumping with more energetic photons, such as e.g. the TH of Ti:sapphire ($\lambda_3 = 266$ nm), is difficult because of the onset of strong two-photon absorption in the nonlinear crystals at the intensities required for the OPA process [67]; generation of tunable UV pulses is nevertheless possible by SHG of the visible OPA [68, 69] or SFG with the FF pulses [70]. Long-wavelength tuning is limited in BBO to 3 μm by the onset of mid-infrared absorption. Other crystals with higher refractive index display a more extended mid-IR transparency, allowing the direct
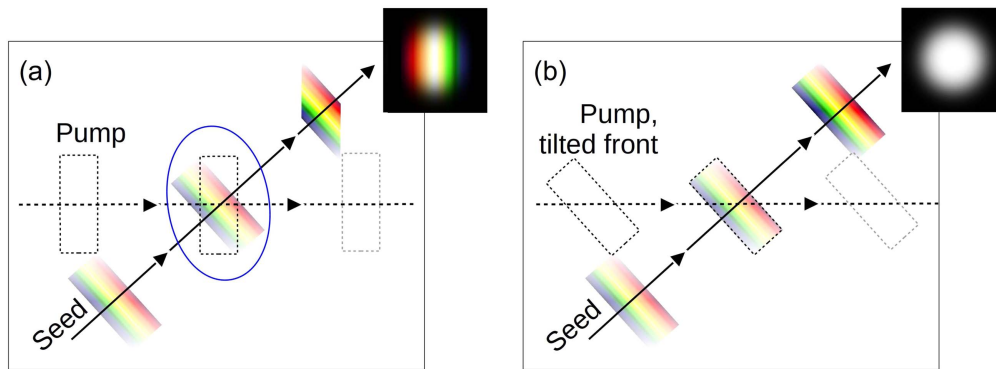
Figure 22. The effect of parametric amplification with large beams: (a) the large spatial chirp arising from the amplification of large beams by non-tilted pump-pulses; (b) homogeneous amplification by a front-tilted pump. Optimum tilting matches the internal non-collinear angle.

generation of mid-IR idler pulses out to a wavelength of $\simeq 5\,\mu$m [71–73]. Examples of these crystals are LiIO$_3$, KNbO$_3$, KTiOPO$_4$ (KTP) or its isomorphs, MgO:LiNbO$_3$, LN and SLT. These crystals are however not transparent in the 5–10 μm region (the fingerprint region), where many molecular vibrational transitions occur. There are crystals with extended mid-IR transparency, such as ZnGeP$_2$ (ZGP), GaSe, AgGaSe$_2$ and AgGaS$_2$ (AGS), but they all display absorption onsets in the visible (0.74 μm for ZGP, 0.65 $\simeq\ \mu$m for GaSe, 0.73 μm for AgGaSe$_2$ and 0.53 μm for AGS) so that they all suffer from two-photon absorption when pumped at 800 nm, preventing the direct generation of mid-IR pulses as the idler of an 800 nm pumped OPA for wavelengths longer than 5 μm. The situation improves slightly at 1030 nm wavelength, which allows pumping of the AGS crystal and direct generation of idler pulses tunable out to 7 μm [74]. However, due to the large GVM between signal and idler, the amplified bandwidth is rather narrow, resulting in pulsewidths of 160 fs or longer. There is a current ongoing research effort in developing powerful sources of ultrashort pulses at $\simeq 2\,\mu$m, based on Ho: or Tm:doped gain media, which would allow direct pumping of mid-IR OPAs based on the above mentioned crystals [75].

The choice of the OPA pump wavelength influences not only the tuning range, but also the gain of the amplification process. On the one hand, the gain scales exponentially with the frequency of the pump pulse. On the other hand, higher pump frequencies typically result in larger temporal walk-off due to the larger GVMs, which limits their interaction length and, correspondingly, the maximum permissible crystal thickness and the resulting gain.

The following simple design criteria can thus be given for the choice of the pump wavelength of an OPA:

D4 Keeping in mind the required OPA wavelength or tuning range, check which pump wavelength allows to achieve it, possibly with the lowest number of frequency conversion steps (SHG, SFG, DFG).

D5 When choosing the pump wavelength, consider also the phase matching bandwidth and the resulting minimum pulse duration, to check whether it complies with the requirement of the application.

D6 It is generally easier to scale in energy OPAs pumped at longer wavelengths (i.e. by the FF of Ti:sapphire or Yb lasers), since the more favourable GVM conditions allow the use of longer crystals; in addition parasitic third order nonlinear effects are reduced due to the scaling of the critical power for self-focusing with λ^2.

Pump pulse energy. The gain of a parametric amplifier depends on the intensity of the pump pulse, as shown by the discussion following equation (2.14). In the pulsed regime, the maximum intensity is at the pulse peak, and depends on the pulse duration, its energy and the beam size. Generally, a very high peak intensity may start spurious nonlinear interactions, such as undesired cascaded second order processes among pump, signal and idler beams, or third order processes such as self phase-modulation, self-focusing and small-scale filamentation. In addition, high intensities may damage the surface of the crystal. The threshold for these processes depends on the nonlinear coefficient and the damage threshold of the crystal. In order to be able to use high pump intensities without the onset of these parasitic processes, it is important to have a spatially clean beam profile, without hot spots. Typically, for BBO the pump pulse energy and spot-size should be chosen to get pump peak intensity of the order of 100–150 GW cm^{-2}.

The pump pulse energy limits the energy of the amplified signal pulses; this is better understood from the corpuscular interpretation of the parametric amplification and the Manley–Rowe equations (equation (2.18)): the annihilation of one pump photon generates one signal and one idler photon, therefore the number of signal (idler) photons generated by the amplification process is related to the total number of the initial photons of the pump. The ratio between the number of output signal and input pump photons is hence a good figure of merit for the efficiency of the amplification process, and is particularly meaningful in low-frequency amplifiers. The conversion ratio typically ranges from 10% in pre-amplification stages to 30% in power amplifiers [76, 77]. In [78], for example, an OPA pumped by 1.03 μm, 640 μJ pulses amplifies 3 μm signal light to 40 μJ energy; while in terms
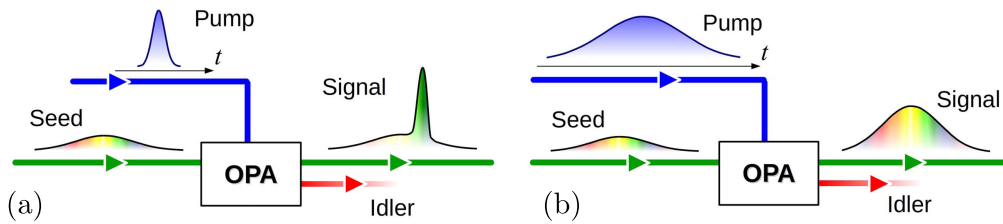
Figure 23. Amplification of a broadband, chirped seed by (a) a short and (b) a long pump. The pump duration influences the bandwidth of the amplified beam.

of pulse energy this means only 6% pump → signal conversion, actually it corresponds to ≃20% converted photons.

For the power amplification stages in a non-collinear interaction geometry care should be taken to match the pulse-fronts of the non-collinear large-diameter pump and signal beams. As shown in figure 22, for untilted pump pulses, due to the non-collinear geometry different portions of the signal spatial profile are temporally overlapped with the pump, and thus amplified, at different times, resulting in a large spatial chirp of the signal [79, 80]. Pulse front tilting can be achieved by the use of a grating [81] or a prism, possibly followed by a telescope for fine tuning of the tilt angle [82].

From these considerations, we can derive the following design criteria for the choice of the pump-pulse energy:

D7 From the target energy of the amplified signal, set the pump energy assuming that the photon conversion efficiency is in the range of 10%–30%.

D8 Choose the pump spot-size and energy at the interaction point that keeps its peak power below the damage threshold of the nonlinear crystal, and below the onset of higher-order processes. The pump size at the nonlinear interaction can be adjusted by a lens or by a telescope.

D9 For high-energy OPAs, where large pump sizes are required to limit the pump peak-power, in the case of non-collinear interaction apply pulse-front tilting to the pump to avoid spatial chirp of the amplified pulse.

Pump pulse duration. The pump pulse duration is often determined by the characteristics of the laser system used to drive the OPA. One important prerequisite is that the pulses are short enough to allow generation of a stable seed pulse by WLC. This is however possible with most commercially available femtosecond laser systems, using sapphire for Ti:sapphire lasers (with duration 100 fs or shorter) and YAG for Yb lasers with longer (200–300 fs) pulsewidths. That said, one should however note that, somewhat counterintuitively, there is no direct relationship between the pump pulse duration and the duration of the shortest OPA pulse. Assuming that an OPA is seeded by a broadband WLC, the minimum pulse duration achievable, which is the TL duration corresponding to the OPA spectrum, is in fact determined by the gain bandwidth of the OPA, which essentially depends on the signal-idler GVM δ_{12} rather than on the pump pulse duration (see section 2.3.2). Broadband OPAs pumped by Ti:sapphire lasers with ≃100 fs pulses and generating sub-10 fs

pulses tunable from 500 nm to 2 μm have been demonstrated [13]. It is possible to achieve sub-10 fs TL pulses from NOPAs even when pumped by Yb sources with 200–300 fs pulsewidth [83]. Using a short pulse to pump the NOPA may actually result in longer amplified pulses, unless measures are taken to temporally stretch the pump pulse. In fact, as shown in figure 23, the pump and seed pulses must be temporally overlapped in order to exchange energy, and the seed, typically produced by WLC generation, is usually temporally chirped by propagation in the generation medium or in other optical elements, so that different colours arrive at different times. Having a short pump pulse will thus result in a limited number of frequency components of the signal overlapping with it and thus in a narrower amplified bandwidth, corresponding to longer OPA pulses. In broadband OPAs, therefore, it is often necessary to temporally stretch the pump pulse, e.g. by propagation in a dispersive glass block [84].

One can thus formulate the following simple design rules:

D10 The duration of the pulses generated by an OPA does not depend on the pump pulse duration; once broadband phase-matching is satisfied, an OPA can generate pulses which are significantly shorter than the pump laser (this is especially important when using OPAs in combination with long-pulse Yb laser sources).

D11 The seed duration must be shorter than or comparable to the pump pulse to ensure their temporal overlap. With short pumps, the seed must be suitably pre-compressed to avoid gain-narrowing. Alternatively, the pump pulse can be temporally stretched.

3.3.2. Nonlinear interaction parameters. Once the pump characteristics have been selected, the parameters of the nonlinear interaction (crystal type, phase-matching type, crystal length) should be appropriately chosen.

Crystal and interaction type. The choice of the nonlinear crystal is determined by the balance of several parameters: the transparency range; the nonlinear coefficients; the nonlinear interaction parameters; the optical damage threshold; the availability and price.

When designing an OPA, the first crystal parameter that should be taken into account is its transparency range: as discussed in section 3.3.1, this determines the tunability range of the OPA.
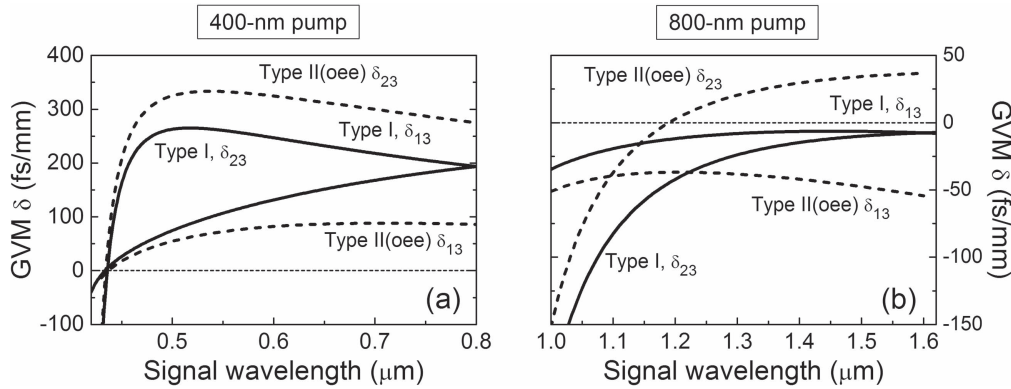
Figure 24. Pump-signal (δ_{13}) and pump-idler (δ_{23}) group velocity mismatch curves for an OPA based on BBO, pumped at (a) 0.8 μm and (b) at 0.4 μm. Both Type I (solid lines) and Type II phase-matching (idler extraordinary, dashed lines) are shown.

As can be seen from equation (2.14) and the following discussion, the parametric gain depends exponentially on the second-order nonlinear coefficient and the figure of merit; using crystals with high nonlinearity and low refractive index is therefore preferable. The low nonlinearity could be compensated for by increasing the peak intensity of the pump or the length of the crystal. However, large peak intensity may lead to higher order detrimental processes or even damage of the crystal surface.

One very important parameter that drives the choice of the crystal is its amplification bandwidth. Broadband operation can be achieved when $\delta_{12} > 0$ in the spectral range of interest; evaluation of δ_{12} for various crystals, polarisation configurations (Type 0, I, II) and pump wavelengths, allows sorting the best candidates for broadband amplification in a specific spectral region. Following this approach, for example, we learn from figure 15 that broadband amplification in the IR spectral range cannot be obtained using 800 nm-pumped BBO with Type-I configuration, since $\delta_{12} < 0$. The same calculation, on the contrary, shows that Type-II configuration exhibits very broadband gain [85]. The capability of a crystal to provide broadband amplification can be assessed by calculating the frequency-dependent gain for various crystal lengths, pump intensities and phase-matching tuning, as shown in figure 16.

BBO offers an excellent combination of the above listed parameters [86] and is therefore the crystal of choice for many OPA applications. It has a broad enough transparency range to allow amplification from 400 nm to 3 μm, as shown in figure 21. Its nonlinear coefficient is moderately high, with $d_{eff} \approx 2$ pm V^{-1} for Type I OPA pumped at 400 nm.

Bismuth triborate (BiB$_3$O$_6$, or BIBO) is a biaxial crystal which possesses extremely large parametric gain bandwidth for degenerate collinear interaction when pumped at 800 nm [76, 87] and UV transparency edge extending to 286 nm [88]. Its main advantage is the high second order nonlinear susceptibility ($d_{eff} = 3.2$ pm V^{-1} for Type-I SHG [89]) and a figure of merit which is twice that of BBO.

Lithium triborate (LiB$_3$O$_5$, LBO) has high damage threshold [90] and small walk-off angle (see next section), which make it suited for the final power amplification stages with long crystal lengths. In addition, it has larger angular

acceptance for a given gain compared to other common nonlinear crystals [91, 92], so that it is best suited with tightly focused beams, and wide transparency range from 160 nm to 2.6 μm. However, this crystal displays a lower nonlinear coefficient, of the order of $d_{31} \approx 0.76$, pm V^{-1} and $d_{32} \approx 0.85$ pm V^{-1} [93].

LN and SLT have IR transparency extended to 5.2 μm and 5.5 μm respectively, which make them suited for amplification in the infrared. For both crystals, the highest element of the nonlinear tensor is d_{33} (27, pm V^{-1} for LN, and -21, pm V^{-1} for SLT), an extremely high nonlinearity which can be only exploited with Type-0 interaction. For this reason, they are typically periodically poled to obtain QPM. LN has low optical and photorefractive damage threshold, which can be increased by doping the crystal with Magnesium–Oxide (MgO) without affecting its high non-linear coefficient. Large aperture MgO:PPLN crystals have been recently manufactured [94], and could be used to increase the pulse-energy of an OPA while keeping the peak-power at low levels. In power stages or booster amplifiers, PPSLT is preferred thanks to its higher damage threshold [95].

The design rules concerning the choice of the crystal type are hence the following:

D12 Choose the crystal according to its transparency range, phase-matching bandwidth and damage threshold.

D13 If the most suitable crystal has low damage threshold, it is better to use a multi stage, large-beam OPA chain.

D14 Identify the plane containing the optical axis of the crystal. This plane defines the ordinary and extraordinary polarisation of all the OPA beams, and also their propagation plane (see figures 6 and 9).

D15 Adjust the polarisations of the pump and seed beams according to the interaction type.

Crystal length. As we discussed in section 2.1, the parametric gain depends exponentially on the crystal length. However, for ultrashort pulses, the amplification occurs only when the pump pulse is temporally overlapped with the signal and the idler. For this reason one parameter that limits the
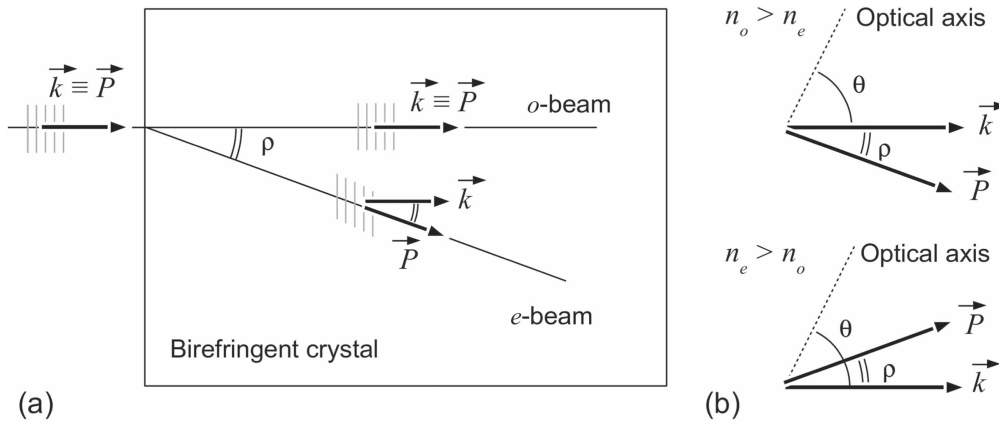
Figure 25. (a) Directions of the wavevector ($\vec{k}$) and of the power flow ($\vec{P}$) due to birefringent walk-off. (b) Walk-off in negative and positive uniaxial crystals.

crystal length is the GVM which, together with the pump pulse duration, determines the pulse splitting length (equation (2.35)). Figure 24 shows examples of GVM curves for a BBO OPA pumped by 0.8 μm (a) and 0.4 μm (b) pulses, respectively. The pulse splitting length, and hence the crystal thickness, could be increased by using long pump pulses; longer crystals can be used also when $\delta_{13} \cdot \delta_{23} < 0$. However another factor limits the interaction length, which is the *spatial walk-off*. This occurs whenever the pulses spatially separate from each other in the transverse direction, hence the interaction length depends on the beam size and the angle between the beams.

In non-collinear amplification, the lateral separation between the beams depends on their (internal) propagation directions, which form an angle of few degrees as shown in figures 10 and 11 for the pump-signal beams, and in figure 14 for the signal-idler fields. Another source of spatial walk-off originates whenever a light beam with *extraordinary* polarisation propagates in a birefringent medium, as shown in figure 25. In this case the direction of the wave vector ($\vec{k}$, normal to the wavefronts) does not coincide with that of the power flow (Poynting vector $\vec{P}$), but forms with it an angle ρ. For the case of a uniaxial crystal we have [1]:

$$\rho(\theta) = \pm\{\arctan[(n_\text{o}/n_\text{e})^2 \tan\theta] - \theta\}, \quad (3.1)$$

where (+) refers to a negative uniaxial crystal ($n_\text{o} > n_\text{e}$) and (−) to a positive one ($n_\text{e} > n_\text{o}$). Birefringent walk-off affects both collinear and non-collinear interactions; in non-collinear configuration, the pump-signal and pump-idler angles may have the same magnitude as ϱ: by properly choosing the direction of the optical axis, the birefringent walk-off can be used to compensate for the non-collinear walk-off. It should be noted that spatial walk-off is absent in Type 0 phase matching, achieved with periodically poled crystals, or when the propagation direction is orthogonal to the optical axis ($\theta = 90°$, non critical phase matching). In both cases, the absence of spatial walk-off enables tighter focusing in the crystal and longer interaction lengths.

The simple rule concerning the crystal length is the following:

D16 Evaluate the optimum crystal length according to the pulse-splitting length and the lateral separation of the beams due to spatial walk-off. The only exception occurs when $\delta_{13} \cdot \delta_{23} < 0$.

3.4. Pulse compression

The third optional sub-system of an OPA is pulse compression, to compensate for the spectral phase accumulated by the amplified pulses, and achieve TL pulse duration. Typically, for visible/near-IR wavelengths, the OPA pulses are positively chirped due to material dispersion introduced by the seed generation process (e.g. by linear propagation of the WLC in the sapphire/YAG plate), by optical elements in the signal path (lenses, beam splitters, spectral filters ...) and by the OPA crystals. For narrow amplified pulse bandwidths (i.e. corresponding to TL pulsewidths of $\simeq$50 fs or longer, see figure 29) the effects of such dispersion are negligible, so that no compression is necessary and the OPA pulses can be used as generated (this does not hold for an OPCPA, in which pulses are stretched to picosecond duration and need to be recompressed in any case, even for modest amplified bandwidths). For broader bandwidths, as typically achieved with a NOPA or a degenerate OPA, pulse compression is necessary to achieve the TL pulse duration. For moderately broad bandwidths, it is sufficient to correct the second order dispersion, or group delay dispersion (GDD, see appendix A.3 for details), while for broader bandwidths, and in particular for sub-10 fs TL pulses, it is also necessary to simultaneously correct for the third order dispersion (TOD).

Several optical systems providing negative dispersion in the visible/near-IR are available (figure 26), including grating pairs, prism pairs, chirped mirrors (CMs) and adaptive optical systems.

Grating pairs [96], see panel (a) are not commonly used with OPAs due to their high losses and the large GDD values that they introduce. The simplest compressor consists of a Brewster-cut prism pair in a folded configuration [97, 98], see panel (b); for a given prisms distance and glass insertion, it can be adjusted to introduce a negative GDD which
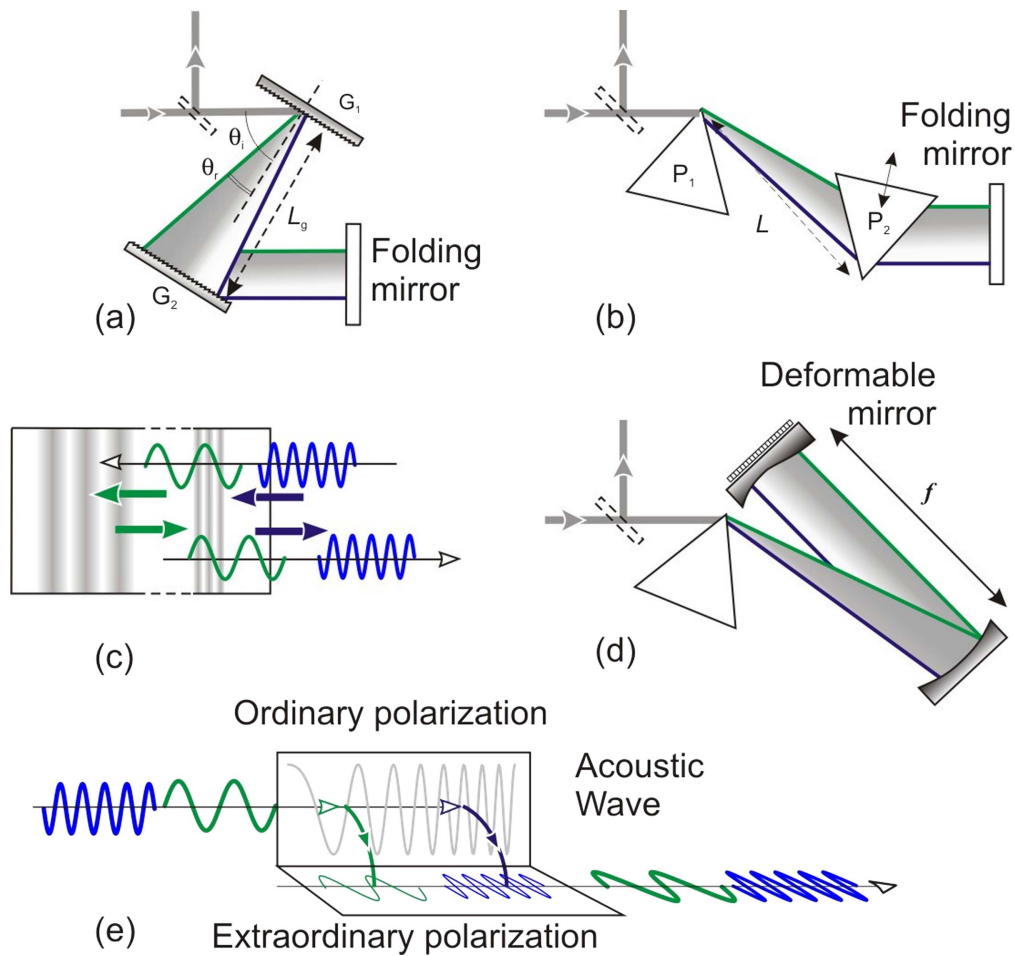
Figure 26. Basic schemes for the manipulation of the spectral phase of a pulse: (a) grating pair; (b) prism pair; (c) chirped mirrors; (d) adaptive pulse shaper, with a deformable mirror in the Fourier plane; (e) acousto-optic programmable dispersive filter.

compensates for the GDD of the OPA pulses, however it simultaneously introduces a large negative TOD, which cannot be independently controlled. Since both GDD and TOD are proportional to the prism tips separation, the ratio TOD/GDD is a characteristic of the prisms material and the wavelength, and can be minimised by choosing materials with low dispersion (such as fused silica, MgF_2 or CaF_2). In this case, however, the prism distance required to achieve a given value of GDD increases. Since it can only correct for GDD but not also for TOD, a simple prism compressor is suitable for TL pulse durations down to $\simeq 20$ fs, but not for broader bandwidths. An additional disadvantage of the prism pair is the fact that the prism distance needs to be changed as the NOPA wavelength is tuned. A better solution consists in multiple bounces on a pair of CMs [99, 100], panel (c), which can be designed to correct simultaneously for both GDD and TOD and ensure either full compression of the ultra-broadband spectrum generated by a NOPA or pulse compression throughout the NOPA tuning range [101]. CMs have the advantage of high throughput and a particularly robust setup, introducing a dispersion that is essentially insensitive to misalignment and depends only on the number of bounces. CMs introduce a dispersion that can only be varied in discrete steps (e.g. GDD $\simeq -50$ fs^2 in the visible range), so that fine

dispersion tuning requires the insertion of some variable amount of material on the beam path, typically a pair of fused silica wedges. The only disadvantage of CMs is their relatively high cost and the need for dedicated design and fabrication procedures, which are not always available in all wavelength ranges, especially in the IR. Finally, pulse compression can be achieved by adaptive optical systems, which employ pulse shapers to provide an arbitrary control of the frequency-dependent spectral phase. Pulse shapers, panel (d), typically use the so-called 4 f arrangement [102], in which, after a dispersive element (a grating or a prism), a lens (or a spherical mirror) performs a spatial Fourier transform which converts the angular dispersion to a spatial separation at the back focal plane, where a phase (and/or intensity) modulator is located. Different phase modulators, based on liquid–crystals [103], acousto-optic modulators [104] or deformable mirrors [105], can be employed. Alternatively, phase modulation can be achieved by an acousto-optic programmable dispersive filter (AOPDF), as shown in panel (e) [106], in which the light wave interacts with a collinearly propagating acoustic wave. The advantage of the AOPDF is its simplicity, as it is inserted inline in the beam path. Pulse shapers have of course the advantage of ultimate flexibility in spectral phase correction, and offer the possibility to compensate for any

dispersion introduced along the beam path before the experiment. However, this flexibility comes at the price of a greatly increased complexity and cost of the device. Pulse shapers are especially important for fine dispersion compensation in multistage, high-energy OPAs, or in OPCPAs, which introduce a large amount of material dispersion which is difficult to accurately compensate by other means [18]. As design criteria for the pulse compression stage one can thus state the following:

D17 Since achieving dispersion compensation to all orders is challenging, it is a good rule to carefully minimise the material dispersion along the signal beam path (e.g. by using thin optical elements and reflective optics), so as to simplify the requirements for the compressor and achieve more robust spectral phase correction.

D18 Whenever possible and available, use CMs due to their superior robustness, alignment insensitivity and broadband spectral phase correction capability.

D19 For moderate OPA pulse bandwidths, for which GDD compensation is sufficient, it is possible to use the simple, low-cost and readily available prism pair compressors.

D20 When using adaptive pulse shapers in multi-stage OPAs, they should be placed before the final power amplification stage, so that this stage can compensate for the inherent losses that they introduce.

D21 When using dielectric optics to steer the beams, make sure that they are GDD-controlled, to avoid the introduction of detrimental chirp.

3.5. Repetition rate

A final important parameter of the OPA is the repetition rate. OPAs can be pumped by laser systems with very different repetition rates, from a few Hz to a few MHz. Very recently, thanks to the very large nonlinear coefficients afforded by periodically poled crystals, it even became possible to directly pump OPAs with the unamplified output of a laser oscillator [107]. There are nowadays sources, such as Yb lasers, which can deliver trains of femtosecond pulses at repetition rates that can be changed from 1 to hundreds of kHz, while keeping approximately the same average power, so that the pulse energy scales inversely to the repetition rate. Note that an OPA design is typically optimised for a given repetition rate and does not tolerate such large variations. In fact an OPA design requires the control of various parameters: (i) the energy and divergence of the pulse driving the WLC generation should always remain constant to guarantee above-threshold, stable operation; (ii) the amplifier pump intensity should be kept at a constant level (of the order of $100 \, \mathrm{GW \, cm^{-2}}$) in order to achieve enough gain while avoiding spurious nonlinear effects. If by varying the repetition rate the pulse energy changes by orders of magnitude (for example it decreases by two orders of magnitude in going from 1 to 100 kHz) the OPA layout needs to be deeply changed to keep the above mentioned parameters (for

example modifying the splitting ratios or changing the beam spot sizes). In case of large variations of repetition rate it might even be necessary to completely revise the OPA design, adding or removing an amplification stage. It may be therefore possible to design an OPA that is optimised for a given repetition rate (for example 10 kHz), and has a limited tuning range (say 3–30 kHz) with sub-optimum performance. Finally, one should consider that, when the OPA is operated with high average powers and high repetition rates, thermal effects may become relevant both in the WLC generation stage and in the OPA stages. In fact, while the OPA process should in principle deposit no energy in the nonlinear medium, as it acts between virtual states, there is always practically a parasitic linear or multiphoton absorption, which becomes more relevant for shorter wavelengths (typically accessed by the pump beam) or in the mid-IR (typically accessed by the idler beam) [108]. Such heat deposition in the crystal may generate transverse temperature gradients leading to beam distortions, deviations from the phase-matching conditions and in extreme cases even catastrophic crystal failure. In summary the following design criteria for the choice of the repetition rate can be given:

D22 The repetition rate is dictated by the requirements of the applications and the OPA design can adapt to it; however there is a limited tolerance to variations of the repetition rate and big changes may require a complete redesign of the OPA.

D23 For high powers and high repetition rates, thermal effects in the WLC generation stage and in the OPA stages should be taken into account.

4. Conclusions

The main goal of this paper is to provide a comprehensive and self-contained introduction to the physical working principles of femtosecond OPAs. As such we hope that it will be useful for a broad readership of PhD students and PostDocs who are not specialists in ultrafast optics, but rather need to use or develop OPAs for applications to physics, chemistry, biology or materials science. We are confident that our treatment will offer to those readers sufficient physical insight to understand the mechanisms governing the operation of the OPAs they use in the lab, and to optimise their performance. At the same time, the paper aims at deriving general design criteria for OPAs, focusing on the following critical aspects: the OPA architecture, the choice of the pump source, the selection of the nonlinear crystal(s) and the design of dispersion compensating optics. These criteria are the result of the authors' experience in designing, building and operating ultrafast OPAs, and we hope that they will be of interest to a more specialised readership, who work on pushing the frontiers of ultrashort pulse generation exploiting the unique properties of OPAs.

Acknowledgments

Appendix A. Linear propagation of ultrashort pulses

In this appendix, we will study the propagation of ultrashort light pulses in absence of nonlinear interaction ($P_{NL}(z, t) = 0$). We will introduce the Fourier transform as a tool to describe linear propagation (A.1), derive the equation for linear pulse propagation (A.2) and briefly discuss the concepts of dispersion and spectral phase (A.3).

A.1. Fourier transform

An ultrashort light pulse can be described both in the *time domain* or in the *frequency domain*; conversion between these domains is possible thanks to the Fourier-transform operator. For a generic electric field $E(z, t)$, we can write (here we will omit the dependence on the spatial coordinate for simplicity):

$$\tilde{E}(\omega) = \mathscr{F}\{E(t)\} = \frac{1}{\sqrt{2\pi}}$$
$$\times \int_{\mathfrak{R}} E(t) \cdot e^{-j\omega t} dt \quad \text{Fourier transform,} \quad \text{(A.1)}$$

$$E(t) = \mathscr{F}^{-1}\{\tilde{E}(\omega)\} = \frac{1}{\sqrt{2\pi}}$$
$$\times \int_{\mathfrak{R}} \tilde{E}(\omega) \cdot e^{j\omega t} d\omega \quad \text{inverse Fourier transform.}$$
$$\text{(A.2)}$$

The Fourier transform is particularly suited for the description of electric-field transients and the propagation of light pulses. Equation (A.2) shows that $E(t)$ can be developed as a superposition of orthogonal harmonic functions $e^{j\omega t}$. In our case, these functions are monochromatic light waves with angular frequencies ω; $\tilde{E}(\omega)$ is the complex coefficient of each wave, and contains information on both its *amplitude* $|\tilde{E}(\omega)|$ and the *phase* $\phi(\omega) = \arg\{\tilde{E}(\omega)\}$. Generally, we call power spectrum (or simply spectrum) the function $|E(\omega)|^2$.

$E(z, t)$ is frequently written in terms of a slowly varying *envelope* function $B(z, t)$ times a traveling optical *carrier* term $\cos(\omega_0 t - k_0 z + \phi)$ at frequency ω_0 and time-dependent phase ϕ. This can also be written in the form:

$$E(z, t) = B(z, t)\cos(\omega_0 t - k_0 z + \phi)$$
$$= \frac{1}{2} A(z, t) e^{j(\omega_0 t - k_0 z)} + \text{c.c.}$$
$$= \mathfrak{R}\{A(z, t) e^{j(\omega_0 t - k_0 z)}\}, \quad \text{(A.3)}$$

where we have introduced the complex amplitude $A(z, t) = B(z, t) e^{j\phi}$. With these definitions and neglecting for the sake of simplicity the z dependence, the average intensity of the field is:

$$\langle E(t)^2 \rangle = \frac{1}{2} |A(t)|^2 \quad \text{(A.4)}$$

and the Fourier transform is:

$$\tilde{E}(\omega) = \mathscr{F}\left\{ \frac{1}{2} A(t) e^{j\omega_0 t} + \text{c.c.} \right\}$$
$$= \frac{1}{2} \tilde{A}(\omega - \omega_0) + \frac{1}{2} \tilde{A}^*(-\omega - \omega_0), \quad \text{(A.5)}$$

where $\tilde{A}(\omega)$ is the Fourier transform of the envelope $A(t)$ and $\tilde{A}^*(\omega)$ is its complex conjugate. Functions $\tilde{E}(\omega)$ and $\tilde{A}(\omega)$ are sketched in figure 27 for the common case in which the bandwidth of the pulse is less than ω_0 [1]. This shows that a field can be fully described through its envelope.

To evaluate how a pulse temporal profile correlates with its spectral content, let's consider, as an example, a pulse with carrier angular frequency ω_0 and Gaussian envelope:

$$E(t) = \frac{1}{2} A_0 e^{-t^2/2\tau^2} e^{j\omega_0 t} + \text{c.c..} \quad \text{(A.6)}$$

The duration of this pulse, calculated as the FWHM of the envelope intensity, is $\Delta T = 2\sqrt{\ln 2} \cdot \tau$. The Fourier transform of its envelope is also Gaussian:

$$\tilde{A}(\omega) = A_0 \tau e^{-\omega^2 \tau^2/2} \quad \text{(A.7)}$$

and the corresponding bandwidth, calculated as the FWHM of $|\tilde{A}(\omega)|^2$, is $\Delta\Omega = 2\sqrt{\ln 2}/\tau$; the time-bandwidth product is hence $\Delta T \cdot \Delta\Omega = 4 \ln 2$. This shows that *the pulse duration is inversely proportional to its bandwidth* and hence an ultrashort pulse has a broad bandwidth, a feature which generally holds for all pulse shapes besides the Gaussian profile shown here. Other examples are shown in [1].

A.2. Linear propagation

We will now show how the Fourier transform operator can be used to study the propagation of a light pulse.

Let's first focus on the differential equation of the propagation. In the linear regime, $P_{NL}(z, t) \simeq 0$ and equation (2.2) becomes:

$$\frac{\partial^2 E(z, t)}{\partial z^2} - \mu_0 \frac{\partial^2 D(z, t)}{\partial t^2} = 0. \quad \text{(A.8)}$$

The linear response ε_r of the medium is time-dependent, so that the electric displacement $D(z, t)$ is [36]:

$$D(z, t) = \varepsilon_0 E(z, t) + P_L(z, t) = \varepsilon_0 \varepsilon_r(t) * E(z, t),$$
$$\text{(A.9)}$$

where $*$ is the convolution symbol. Equation (A.8) becomes:

$$\frac{\partial^2 E(z, t)}{\partial z^2} - \frac{1}{c_0^2} \frac{\partial^2}{\partial t^2}[\varepsilon_r(t) * E(z, t)] = 0, \quad \text{(A.10)}$$

where $c_0 = 1/\sqrt{\varepsilon_0 \mu_0}$ is the speed of light in vacuum. Finding general solutions of this equation is particularly straightforward in the frequency domain; let's first take the Fourier
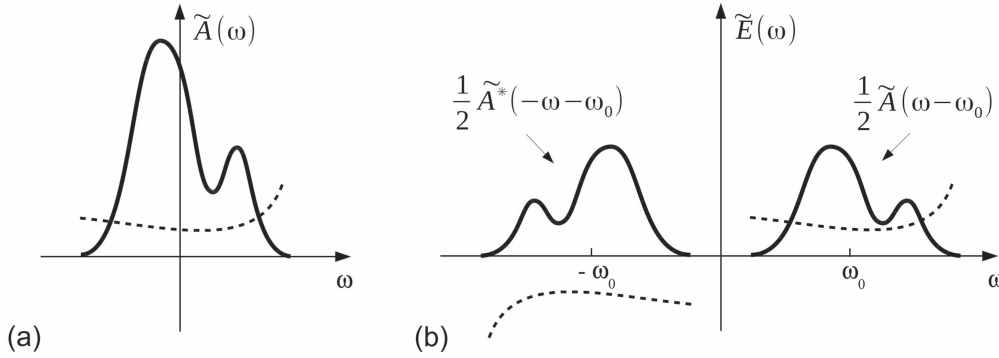
Figure 27. Fourier transform of the envelope $A(t)$ (a) and of the complete field $E(t)$ (b). Solid lines: absolute value; dashed lines: phase.

transform of both sides of the differential equation:

$$\frac{\partial^2 \tilde{E}(z, \omega)}{\partial z^2} + \frac{\omega^2}{c_0^2} \cdot n(\omega)^2 \tilde{E}(z, \omega) = 0, \qquad (A.11)$$

where $n(\omega)^2 = \tilde{\varepsilon}(\omega) = \mathscr{F}\{\varepsilon_r(t)\}$ is the Fourier transform of $\varepsilon_r(t)$ and $n(\omega)$ is the frequency-dependent *refractive index* of the medium. The solution of equation (A.11) for each frequency component ω is the linear combination of progressive and regressive waves with complex amplitudes $E_p(\omega)$ and $E_r(\omega)$ respectively:

$$\tilde{E}(z, \omega) = \tilde{E}_p(\omega)\mathrm{e}^{-jk(\omega)z} + \tilde{E}_r(\omega)\mathrm{e}^{+jk(\omega)z}, \qquad (A.12)$$

where we have introduced the wavenumber $k(\omega) = \omega/c_0 \cdot n(\omega)$. In the case of a progressive wave, the field in the time domain is obtained by back Fourier Transform (equation (A.2)):

$$E_{\mathrm{out}}(z, t) = \frac{1}{\sqrt{2\pi}} \int_{\mathfrak{R}} \tilde{E}_p(\omega)\mathrm{e}^{-jk(\omega)z} \cdot \mathrm{e}^{j\omega t}\mathrm{d}\omega$$
$$= \frac{1}{\sqrt{2\pi}} \int_{\mathfrak{R}} \tilde{E}_{\mathrm{in}}(\omega) \cdot \mathrm{e}^{j[\omega t - k(\omega)z]}\mathrm{d}\omega. \qquad (A.13)$$

Here $\tilde{E}_{\mathrm{in}}(\omega)$ is the boundary condition, corresponding to the Fourier transform of $E_{\mathrm{in}}(0, t)$.

This equation expresses mathematically an intuitive concept: at each longitudinal coordinate z, a propagating pulse is a superposition of traveling monochromatic waves with angular frequency ω and wavenumber $k(\omega)$. The quantity:

$$k(\omega)z = n(\omega)\frac{\omega}{c_0}z = \phi(\omega) \qquad (A.14)$$

is the *spectral phase* accumulated by each monochromatic wave during propagation. The dependence of ϕ on $n(\omega)$ is responsible of pulse dispersion, that we will now study in detail.

A.3. Spectral phase and dispersion

The spectral phase $\phi(\omega)$ conveys important information about the propagation of a pulse. Since ϕ depends on ω, during propagation each monochromatic component of

equation (A.13) accumulates its own phase delay:

$$\tau_p = \frac{\phi(\omega)}{\omega} \qquad \text{phase delay.} \qquad (A.15)$$

To understand how such frequency-dependent delay influences the propagation of a pulse, let's approximate $\phi(\omega)$ to the first order of a Taylor expansion around the pulse carrier frequency ω_0:

$$\phi(\omega) \simeq \phi(\omega_0) + \frac{\partial \phi}{\partial \omega}\bigg|_{\omega_0} (\omega - \omega_0)$$
$$= \phi_0 + \phi_0' \cdot (\omega - \omega_0) \qquad (A.16)$$

and substitute it into equation (A.13); we obtain an approximate expression of the output pulse:

$$E_{\mathrm{out}}(t) \simeq \frac{1}{\sqrt{2\pi}} \int_{\mathfrak{R}} \tilde{E}_{\mathrm{in}}(\omega) \cdot \mathrm{e}^{j\omega t} \cdot \mathrm{e}^{-j[\phi_0 + \phi_0' \cdot (\omega - \omega_0)]}\mathrm{d}\omega$$
$$= \mathrm{e}^{-j\phi_0} \cdot \mathrm{e}^{-j\phi_0'\omega_0} \frac{1}{\sqrt{2\pi}} \times \int_{\mathfrak{R}} \tilde{E}_{\mathrm{in}}(\omega) \cdot \mathrm{e}^{j[t-\phi_0']\omega}\mathrm{d}\omega$$
$$= (...)E_{\mathrm{in}}(t - \phi_0'). \qquad (A.17)$$

The result shows that $|E_{\mathrm{out}}| = |E_{\mathrm{in}}(t - \phi_0')|$, i.e. $|E_{\mathrm{out}}(t)|$ is a delayed replica of the initial $|E_{\mathrm{in}}(t)|$. This delay is known as the group delay (GD):

$$\mathrm{GD} = \phi_0' = \frac{\partial \phi}{\partial \omega}\bigg|_{\omega_0} = \tau_p\left[1 + \frac{\omega_0}{n}\frac{\partial n}{\partial \omega}\bigg|_{\omega_0}\right]. \qquad (A.18)$$

The GD is the delay of a wavepacket centered around ω_0 after its propagation in a dispersive medium. Since the refractive index n varies with ω according to the material dispersion, $\partial n/\partial \omega \neq 0$, and $\mathrm{GD} \neq \tau_p$. If $\phi(\omega)$ is expanded to higher orders in ω similarly to equation (A.16), the following parameters can be defined:

$$\mathrm{GDD} = \frac{\partial \mathrm{GD}}{\partial \omega}\bigg|_{\omega_0} = \frac{\partial^2 \phi}{\partial \omega^2}\bigg|_{\omega_0}$$

group delay dispersion, $\qquad (A.19)$

$$\mathrm{TOD} = \frac{\partial \mathrm{GDD}}{\partial \omega}\bigg|_{\omega_0} = \frac{\partial^3 \phi}{\partial \omega^3}\bigg|_{\omega_0}$$

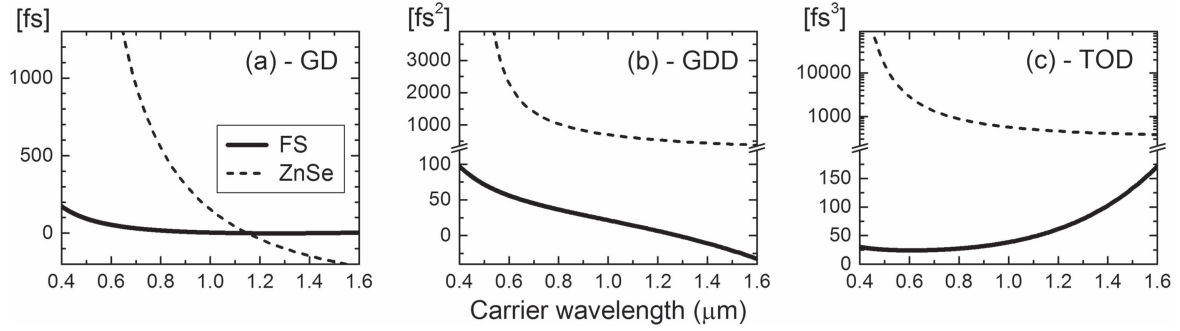third order dispersion. $\qquad (A.20)$

Figure 28. Dispersion of 1 mm thick plates of fused silica (FS) and zinc selenide (ZnSe).

Dispersion can be better understood by expanding the group delay:

$$\mathrm{GD}(\omega) \simeq \mathrm{GD}(\omega_0) + \mathrm{GDD}(\omega_0) \cdot (\omega - \omega_0)$$
$$+ \frac{1}{2}\mathrm{TOD}(\omega_0) \cdot (\omega - \omega_0)^2 + \cdots. \quad (A.21)$$

The higher order terms in the expansion, proportional to GDD and TOD, describe the frequency dependence of the group delay and hence are responsible for the distortion of the pulse shape: the GDD leads to pulse broadening, while a strong TOD gives rise to an asymmetric temporal profile and multiple delayed replicas. As an example, figure 28 plots the frequency-dependent GD, GDD and TOD introduced by propagation in 1 mm thick fused silica and zinc selenide plates. Due to the onset of electronic absorption closer to the visible spectral range, zinc selenide has much stronger dispersion than fused silica, which results in larger relative delay of the components of a pulse during propagation. To quantify the effect of the GDD, let's again consider the Gaussian pulse of equation (A.6). We can calculate the temporal profile of the pulse resulting from pure second order dispersion (GDD $\neq$ 0, TOD = 0) by following the approach based on the Fourier transform, as we did for equation (A.17). The resulting pulse still has a Gaussian shape, with the following value of τ_{out}:

$$\tau_{\mathrm{out}} = \tau\left[1 + \left(\frac{\mathrm{GDD}}{\tau^2}\right)^2\right]^{1/2}. \quad (A.22)$$

This equation shows the main effect of GDD on the pulse width. When GDD $\gg \tau^2$ (large dispersion, or short pulse), equation (A.22) can be approximated as $\tau_{\mathrm{out}} \approx \mathrm{GDD}/\tau$, indicating that the shorter the pulsewidth τ, the more it is susceptible to dispersive broadening. This can be intuitively understood by considering that a short pulse contains many frequencies, which travel with different group velocities in the medium. When GDD $\ll \tau^2$ (small dispersion, or long pulse), $\tau_{\mathrm{out}} \approx \tau$, and the pulse does not get significantly longer. To illustrate the effects of pulse broadening, figure 29 plots ΔT, as a function of the input pulsewidth, of a Gaussian pulse at 800 nm carrier wavelength after propagation in a 1 mm thick fused silica and zinc selenide block. For the case of fused silica, due to the low value of the GDD, the output pulsewidth is unaffected by dispersion down to a duration of approximately 10 fs. For ZnSe, on the other hand, due to the large
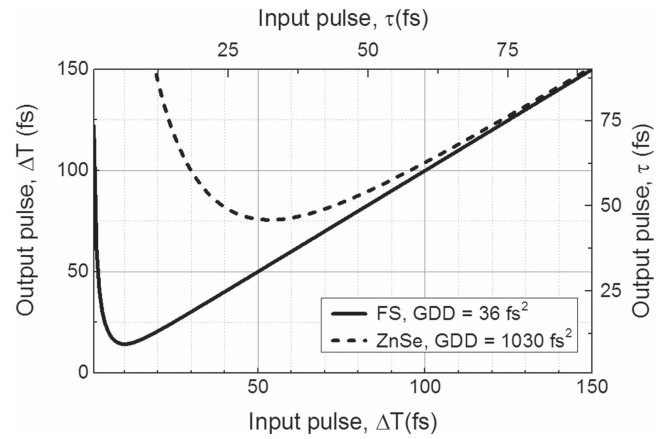

Figure 29. Duration of a Gaussian pulse, before and after propagation in a 1 mm thick plate of fused silica (FS) and zinc selenide (ZnSe). The dispersion is evaluated at carrier wavelength $\lambda = 800$ nm.

value of GDD, temporal broadening manifests itself already at much longer pulsewidths.

Before concluding this section, we finally introduce two more parameters which will be useful for the description of pulse propagation. Since $\phi(\omega) = kz$, the first, second and third derivatives of $\phi(\omega)$ can be calculated as a function of the wavenumber $k(\omega)$, the group delay is:

$$\mathrm{GD} = \frac{\partial \phi}{\partial \omega}\bigg|_{\omega_0} = \frac{\partial k}{\partial \omega}\bigg|_{\omega_0} z = z/v_{\mathrm{g}}, \quad (A.23)$$

where

$$v_{\mathrm{g}} = \frac{\partial \omega}{\partial k}\bigg|_{\omega_0} \quad (A.24)$$

is the group velocity. Analogously one can write:

$$\mathrm{GDD} = \frac{\partial^2 \phi}{\partial \omega^2}\bigg|_{\omega_0} = \frac{\partial^2 k}{\partial \omega^2}\bigg|_{\omega_0} z = z \cdot \mathrm{GVD}, \quad (A.25)$$

where

$$\mathrm{GVD} = \frac{\partial}{\partial \omega}\frac{1}{v_{\mathrm{g}}}\bigg|_{\omega_0} = \frac{\partial^2 k}{\partial \omega^2}\bigg|_{\omega_0} \quad (A.26)$$

is the group velocity dispersion. Note that both v_{g} and GVD are independent from the propagation length z.

In parametric amplification, pump, signal and idler pulses have different carrier wavelengths and group velocities; for this reason, they accumulate distinct group delays after propagating in a medium with thickness z. When two pulses (namely i and j) enter simultaneously in the medium, their relative group delay is:

$$\mathrm{GD}_i - \mathrm{GD}_j = \left(\frac{1}{v_{gi}} - \frac{1}{v_{gj}}\right) z = \delta_{ij} z. \tag{A.27}$$

This delay is responsible for the so-called *temporal walk-off*, which leads to a reduction of the pulses' temporal overlap. The walk-off is proportional to the parameter δ_{ij}, named GVM, and determines the effective interaction length in parametric amplification with broadband pulses, as will be discussed later.

Appendix B. Numeric calculation of phase-matching angle

In a nonlinear interaction based on birefringence, determining the phase-matching angle is necessary in order to suitably design an OPA. However, in some cases the calculation is not straightforward, and numerical methods are required. In this section we will show some methods to find the phase-matching angle.

B.1. Collinear interaction

For birefringent phase matching, the phase-matching angle can be calculated following approach [27]. If we define:

$$\begin{aligned} A = n_{o1}/\lambda_1 \quad B = n_{o2}/\lambda_2 \quad C = n_{o3}/\lambda_3 \\ D = n_{e1}/\lambda_1 \quad E = n_{e2}/\lambda_2 \quad F = n_{e3}/\lambda_3 \end{aligned} \tag{B.1}$$

and

$$\begin{aligned} U = \left(\frac{A+B}{C}\right)^2 \quad W = \left(\frac{A+B}{F}\right)^2 \quad R = \left(\frac{A+B}{D+B}\right)^2 \\ Q = \left(\frac{A+B}{A+E}\right)^2 \quad S = \left(\frac{A+B}{D+E}\right)^2 \quad V = \left(\frac{B}{C-A}\right)^2 \\ Y = \left(\frac{B}{E}\right)^2 \qquad T = \left(\frac{A}{C-B}\right)^2 \quad Z = \left(\frac{A}{D}\right)^2 \end{aligned} \tag{B.2}$$

the phase-matching angles θ_m for the various configurations are:

$$\begin{aligned} \tan^2\theta_{ooe} = \frac{1-U}{W-1} \quad \tan^2\theta_{eeo} \approx \frac{1-U}{U-S} \\ \tan^2\theta_{eoe} \approx \frac{1-U}{W-R} \quad \tan^2\theta_{oee} \approx \frac{1-U}{W-Q} \\ \tan^2\theta_{oeo} = \frac{1-V}{V-Y} \quad \tan^2\theta_{eoo} = \frac{1-T}{T-Z}. \end{aligned} \tag{B.3}$$

These expressions are exact for interactions with only one extraordinary beam. For the other cases, starting from these values we can determine highly accurate values of θ_m by numerical methods. One approach is to evaluate the wave–
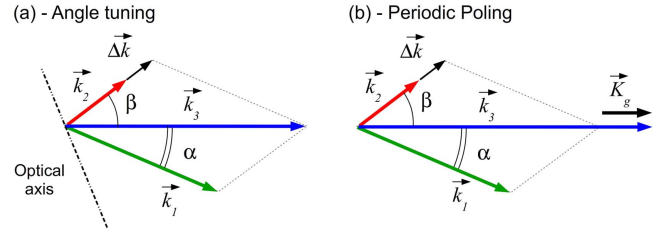

Figure 30. Phase-vector mismatch in non-collinear OPAs, for birefringent (a) and QPM (b) phase matching.
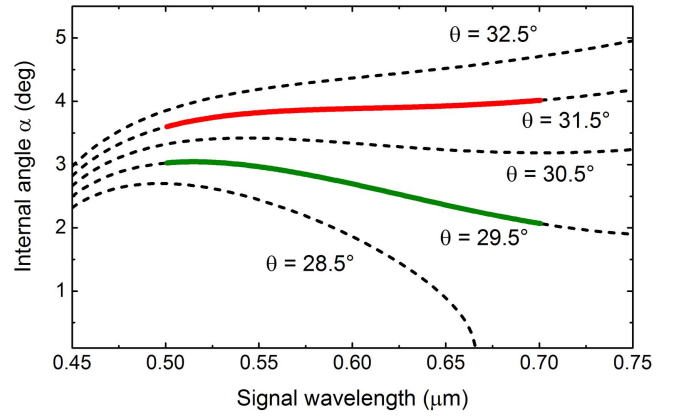

Figure 31. Phase-matched amplification direction α at some values of θ, for a 400 nm-pumped BBO-based visible OPA.

vector mismatch function $\Delta k(\theta) = k_3 - k_2 - k_1$ in a neighborhood of the approximate angles from equation (B.3), and to apply numeric root-finding algorithms (such as bisection or false position methods) to find θ_m giving $\Delta k = 0$.

B.2. Non-collinear interaction

In the non-collinear geometry, the phase-matching angle also depends on the angle α between the pump and the signal. Since the collinear configuration, that we already discussed, can be seen as a non-collinear geometry in which $\alpha = 0$, the calculation of θ_m follows the same method. In figure 30(a) we show the wave–vectors for the mismatched interaction of figure 8(a), together with the geometrical meaning of $\Delta\vec{k}$. To find θ_m, one approach is to evaluate $|\Delta\vec{k}|$ as a function of θ, and then numerically search for its root. In practice, for a generic θ and for a given interaction Type (Type I or Type II) and angle α, one calculates in sequence n_1 and $|\vec{k}_1|$; n_3 and $|\vec{k}_3|$; the angle $\beta(\theta)$, n_2 and $|\vec{k}_2|$; $|\Delta\vec{k}(\theta)|$ and its root θ_m fulfilling $|\Delta\vec{k}(\theta_m)| = 0$. Also in the non-collinear case, a good initial guess for θ is provided by equation (B.3).

A similar numerical approach could be followed for non-collinear QPM, as an alternative approach to the direct solution of equation (2.32). In this case, the wave–vectors for the mismatched interaction are arranged as in figure 30(b). By first evaluating $|\Delta\vec{k}|$ as a function of Λ, one can numerically find the roots Λ_m leading to $|\Delta\vec{k}| = 0$.

For both birefringent phase-matching and QPM, we note that this numerical approach could also be used to find the
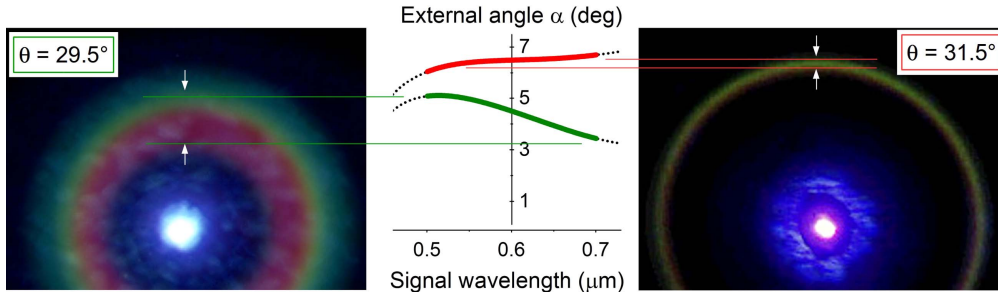
Figure 32. Experimental PSF rings obtained from 400 nm-pumped BBO crystals, for $\theta = 29.5°$ and $\theta = 31.5°$. The central panel shows the calculated external amplification directions, corresponding to red and green internal angles α reported in figure 31.

Table 2. The effective nonlinear coefficient d_{eff} as a function of the uniaxial crystal point group, the polarisation configuration and the crystallographic angles θ and φ, as defined according to convention IEEE/ansi Std 176-1987.

Class point	Nonlinear coefficient d_{eff}	
	Two ordinary beams ooe, oeo, eoo	Two extraordinary beams eeo, eoe, oee
4, 4 mm, 6, 6 mm	$d_{15} \sin\theta$	0
$\bar{6}$ m2	$-d_{22} \cos\theta \sin 3\varphi$	$d_{22} \cos^2\theta \cos\varphi$
3 m	$d_{31} \sin\theta - d_{22} \cos\theta \sin 3\varphi$	$d_{22} \cos^2\theta \cos 3\varphi$
$\bar{6}$	$(d_{11} \cos 3\varphi - d_{22} \sin 3\varphi)\cos\theta$	$(d_{11} \sin 3\varphi + d_{22} \cos 3\varphi)\cos^2\theta$
3	$(d_{11} \cos 3\varphi - d_{22} \sin 3\varphi)\cos\theta + d_{15} \sin\theta$	$(d_{11} \sin 3\varphi + d_{22} \cos 3\varphi)\cos^2\theta$
32	$d_{11} \cos\theta \cos 3\varphi$	$d_{11} \cos^2\theta \sin 3\varphi$
$\bar{4}$	$-(d_{14} \sin 2\varphi + d_{15} \cos 2\varphi)\sin\theta$	$(d_{14} \cos 2\varphi - d_{15} \sin 2\varphi)\sin 2\theta$
$\bar{4}$2 m	$d_{36} \sin\theta \sin 2\varphi$	$d_{36} \sin 2\theta \cos 2\varphi$

phase-matched amplification direction α for a given value of θ or Λ. The angle α is the emission direction of PSF light, generated by the unseeded OPA. The calculation of α requires to evaluate Δk as a function of the non-collinear angle (in the neighborhood of $\alpha = 0$) and to find its roots. The angle α evaluated inside the BBO crystal for a 400 nm-pumped visible NOPA is shown in figure 31; the red line is almost constant in the visible spectral range, and corresponds to the emission direction of a broadband amplifier in the 500–700 nm range. For all directions, the corresponding external angle can be evaluated by Snell's law: in figure 32 we show the external angles for the red and green internal lines. The angle α is the emission direction of PSF light, generated by the unseeded OPA. Note that the angles are in very good agreement with the pictures of the experimental PSF rings.

B.3. The nonlinear effective coefficient

In this section we briefly discuss the nonlinear effective coefficient d_{eff}; this parameter depends on the polarisation of the fields, their propagation direction, the crystallographic point group of the medium and the presence of absorption bands. Whenever all three fields (pump, signal and idler) lie in a region without absorption, Kleinmann's symmetry conditions [109] can be applied to some elements of the nonlinear susceptibility tensor, so that $d_{12} = d_{26}$, $d_{13} = d_{35}$, $d_{14} = d_{36} = d_{25}$, $d_{21} = d_{16}$, $d_{24} = d_{32}$, $d_{31} = d_{15}$ and $d_{32} = d_{24}$; the resulting values of d_{eff} for uniaxial crystals are summarised in table 2 [27, 28].

The propagation direction of the fields is related to two crystallographic angles, θ and φ: θ is the angle between the optical axis and the direction of the k vector (see figure 6), and is strictly determined by the phase-matching condition, as we will discuss in the following. φ, on the other hand, is related to the crystal orientation and does not influence phase matching for the case of a uniaxial crystal: it is selected in order to maximise d_{eff} for Type I or Type II interaction. For example, BBO belongs to class *3m* therefore d_{eff} is maximised for Type I (ooe) interaction when $\varphi = 90° + n120°$ and for Type II (eoe, oee) when $\varphi = n120°$; hence Type I or Type II cystals have different values of φ and cannot be interchanged. We emphasise that, while there is an agreed convention for the definition of θ, there are different conventions for the angle φ: for the values of table 2 we applied convention IEEE/ansi Std 176-1987 [110], the most commonly used one by the facilities that grow crystals. However, some companies use other conventions for the crystallographic axis. For this reason it's better to specify the interaction Type rather than φ when purchasing a crystal.

References

[1] Weiner A 2011 *Ultrafast Optics* (*Wiley Series in Pure and Applied Optics*) (New York: Wiley)

[2] Fork R L, Greene B I and Shank C V 1981 Generation of optical pulses shorter than 0.1 psec by colliding pulse mode locking *Appl. Phys. Lett.* **38** 671–2

[3] Backus S, Durfee C G, Murnane M M, Margaret M and Kapteyn H C 1998 High power ultrafast lasers *Rev. Sci. Instrum.* **69** 1207–23

[4] Eidam T, Hanf S, Seise E, Andersen T V, Gabler T, Wirth C, Schreiber T, Limpert J and Tünnermann A 2010 Femtosecond fiber CPA system emitting 830 W average output power *Opt. Lett.* **35** 94–6

[5] Russbueldt P, Mans T, Weitenberg J, Hoffmann H D and Poprawe R 2010 Compact diode-pumped 1.1 kW Yb:YAG Innoslab femtosecond amplifier *Opt. Lett.* **35** 4169–71

[6] Saraceno C J, Emaury F, Heckl O H, Baer C R E, Hoffmann M, Schriber C, Golling M, Südmeyer T and Keller U 2012 275 W average output power from a femtosecond thin disk oscillator operated in a vacuum environment *Opt. Express* **20** 23535–41

[7] Zewail A H 2000 Femtochemistry: atomic-scale dynamics of the chemical bond *J. Phys. Chem.* A **104** 5660–94

[8] Cerullo G, Manzoni C, Luer L and Polli D 2007 Time-resolved methods in biophysics: IV. Broadband pump–probe spectroscopy system with sub-20 fs temporal resolution for the study of energy transfer processes in photosynthesis *Photochem. Photobiol. Sci.* **6** 135–44

[9] Krausz F and Ivanov M 2009 Attosecond physics *Rev. Mod. Phys.* **81** 163–234

[10] Popmintchev T *et al* 2012 Bright coherent ultrahigh harmonics in the keV x-ray regime from mid-infrared femtosecond lasers *Science* **336** 1287–91

[11] Giordmaine J A and Miller R C 1965 Tunable coherent parametric oscillation in LiNO₃ at optical frequencies *Phys. Rev. Lett.* **14** 973–6

[12] Baumgartner R A and Byer R 1979 Optical parametric amplification *IEEE J. Quantum Electron.* **15** 432–44

[13] Brida D, Manzoni C, Cirmi G, Marangoni M, Bonora S, Villoresi P, De Silvestri S and Cerullo G 2010 Few-optical-cycle pulses tunable from the visible to the mid-infrared by optical parametric amplifiers *J. Opt.* **12** 013001

[14] Strickland D and Mourou G 1985 Compression of amplified chirped optical pulses *Opt. Commun.* **56** 219–21

[15] Dubietis A, Jonušauskas G and Piskarskas A 1992 Powerful femtosecond pulse generation by chirped and stretched pulse parametric amplification in {BBO} crystal *Opt. Commun.* **88** 437–40

[16] Fattahi H *et al* 2014 Third-generation femtosecond technology *Optica* **1** 45–63

[17] Witte S and Eikema K S E 2012 Ultrafast optical parametric chirped-pulse amplification *IEEE J. Sel. Top. Quantum Electron.* **18** 296–307

[18] Herrmann D, Veisz L, Tautz R, Tavella F, Schmid K, Pervak V and Krausz F 2009 Generation of sub-three-cycle, 16 TW light pulses by using noncollinear optical parametric chirped-pulse amplification *Opt. Lett.* **34** 2459–61

[19] Boyd R W 2003 *Nonlinear Optics* (New York: Academic)

[20] Shen Y R 1984 *Principles of Nonlinear Optics* (New York: Wiley)

[21] Arisholm G 1997 General numerical methods for simulating second-order nonlinear interactions in birefringent media *J. Opt. Soc. Am.* B **14** 2543–9

[22] Manzoni C, Cirmi G, Brida D, De Silvestri S and Cerullo G 2009 Optical-parametric-generation process driven by femtosecond pulses: timing and carrier-envelope phase properties *Phys. Rev.* A **79** 033818

[23] Yakovlev V V, Kohler B and Wilson K R 1994 Broadly tunable 30 fs pulses produced by optical parametric amplification *Opt. Lett.* **19** 2000–2

[24] Armstrong J A, Bloembergen N, Ducuing J and Pershan P S 1962 Interactions between light waves in a nonlinear dielectric *Phys. Rev.* **127** 1918–39

[25] Ulbricht R, Hendry E, Shan J, Heinz T F and Bonn M 2011 Carrier dynamics in semiconductors studied with time-resolved terahertz spectroscopy *Rev. Mod. Phys.* **83** 543–86

[26] Manley J M and Rowe H E 1956 Some general properties of nonlinear elements: I. General energy relations *Proc. IRE* **44** 904–13

[27] Dmitriev V G, Gurzadyan G G, Nikogosyan D N and Lotsch H K V 1999 Optics of nonlinear crystals *Handbook of Nonlinear Optical CrystalsSpringer Series in Optical Sciences* vol 64 (Berlin: Springer) pp 3–66

[28] Zernike F and Midwinter J E 1973 *Applied Nonlinear Optics* (New York: Wiley)

[29] Gale G M, Cavallari M, Driscoll T J and Hache F 1995 Sub-20 fs tunable pulses in the visible from an 82 MHz optical parametric oscillator *Opt. Lett.* **20** 1562–4

[30] Franken P A and Ward J F 1963 Optical harmonics and nonlinear phenomena *Rev. Mod. Phys.* **35** 23–39

[31] Hum D S and Fejer M M 2007 Quasi-phasematching *C. R. Phys.* **8** 180–98 Recent advances in crystal opticsAvancées récentes en optique cristalline

[32] Cirmi G, Brida D, Manzoni C, Marangoni M, De Silvestri S and Cerullo G 2007 Few-optical-cycle pulses in the near-infrared from a noncollinear optical parametric amplifier *Opt. Lett.* **32** 2396–8

[33] Wilhelm T, Piel J and Riedle E 1997 Sub-20 fs pulses tunable across the visible from a blue-pumped single-pass noncollinear parametric converter *Opt. Lett.* **22** 1494–6

[34] Cerullo G, Nisoli M and Silvestri S De 1997 Generation of 11 fs pulses tunable across the visible by optical parametric amplification *Appl. Phys. Lett.* **71** 3616–8

[35] Shirakawa A and Kobayashi T 1998 Noncollinearly phase-matched femtosecond optical parametric amplification with a 2000 cm1 bandwidth *Appl. Phys. Lett.* **72** 147–9

[36] Akhmanov S A, Vysloukh V A and Chirkin A S 1992 *Optics of Femtosecond Laser Pulses* 1st edn (New York: American Institute of Physics)

[37] Nisoli M, Danielius R, Piskarskas A, De Silvestri S, Magni V, Valiulis G, Varanavicius A and Svelto O 1994 Highly efficient parametric conversion of femtosecond Ti:sapphire laser pulses at 1 kHz *Opt. Lett.* **19** 1973–5

[38] Cundiff S T and Ye J 2003 Colloquium : femtosecond optical frequency combs *Rev. Mod. Phys.* **75** 325–42

[39] Baltuška A *et al* 2003 Attosecond control of electronic processes by intense light fields *Nature* **421** 611–5

[40] Jones D J, Diddams S A, Ranka J K, Stentz A, Windeler R S, Hall J L and Cundiff S T 2000 Carrier-envelope phase control of femtosecond mode-locked lasers and direct optical frequency synthesis *Science* **288** 635–9

[41] Wirth A *et al* 2011 Synthesized light transients *Science* **334** 195–200

[42] Sansone G *et al* 2006 Isolated single-cycle attosecond pulses *Science* **314** 443

[43] Goulielmakis E *et al* 2008 Single-cycle nonlinear optics *Science* **320** 1614–7

[44] Baltuška A, Fuji T and Kobayashi T 2002 Controlling the Carrier-envelope phase of ultrashort light pulses with optical parametric amplifiers *Phys. Rev. Lett.* **88** 133901

[45] Cerullo G, Baltuška A, Mücke O D and Vozzi C 2011 Few-optical-cycle light pulses with passive carrier-envelope phase stabilization *Laser Photon. Rev.* **5** 323–51

[46] Baltuška A, Fuji T and Kobayashi T 2002 Self-referencing of the carrier-envelope slip in a 6 fs visible parametric amplifier *Opt. Lett.* **27** 1241–3

[47] Wong S T, Plettner T, Vodopyanov K L, Urbanek K, Digonnet M and Byer R L 2008 Self-phase-locked degenerate femtosecond optical parametric oscillator *Opt. Lett.* **33** 1896–8

[48] Nabors C D, Yang S T, Day T and Byer R L 1990 Coherence properties of a doubly resonant monolithic optical parametric oscillator *J. Opt. Soc. Am.* B **7** 815

[49] Manzoni C, Moses J, Kaertner F X and Cerullo G 2011 Excess quantum noise in optical parametric chirped-pulse amplification *Opt. Express* **19** 8357–66

[50] Huang S-W, Moses J and Kärtner F X 2012 Broadband noncollinear optical parametric amplification without angularly dispersed idler *Opt. Lett.* **37** 2796–8

[51] Cerullo G and De Silvestri S 2003 Ultrafast optical parametric amplifiers *Rev. Sci. Instrum.* **74** 1–8

[52] Harris S E, Oshman M K and Byer R L 1967 Observation of tunable optical parametric fluorescence *Phys. Rev. Lett.* **18** 732–4

[53] Marangoni M, Osellame R, Ramponi R, Cerullo G, Steinmann A and Morgner U 2007 Near-infrared optical parametric amplifier at 1 MHz directly pumped by a femtosecond oscillator *Opt. Lett.* **32** 1489–91

[54] Linnenbank H and Linden S 2014 High repetition rate femtosecond double pass optical parametric generator with more than 2 W tunable output in the NIR *Opt. Express* **22** 18072–7

[55] Moses J *et al* 2009 Highly stable ultrabroadband mid-IR optical parametric chirped-pulse amplifier optimized for superfluorescence suppression *Opt. Lett.* **34** 1639–41

[56] Moses J, Manzoni C, Huang S-W, Cerullo G and Kaertner F X 2009 Temporal optimization of ultrabroadband high-energy OPCPA *Opt. Express* **17** 5540–55

[57] Alfano R R and Shapiro S L 1970 Emission in the region 4000 to 7000 Å Via four-photon coupling in glass *Phys. Rev. Lett.* **24** 584–7

[58] Gaeta A L 2000 Catastrophic collapse of ultrashort pulses *Phys. Rev. Lett.* **84** 3582–5

[59] Bradler M, Baum P and Riedle E 2009 Femtosecond continuum generation in bulk laser host materials with sub-J pump pulses *Appl. Phys.* B **97** 561–74

[60] Reed M K, Steiner-Shepard M K, Armas M S and Negus D K 1995 Microjoule-energy ultrafast optical parametric amplifiers *J. Opt. Soc. Am.* B **12** 2229–36

[61] Jukna V, Galinis J, Tamosauskas G, Majus D and Dubietis A 2014 Infrared extension of femtosecond supercontinuum generated by filamentation in solid-state media *Appl. Phys.* B **116** 477–83

[62] Huber R, Satzger H, Zinth W and Wachtveitl J 2001 Noncollinear optical parametric amplifiers with output parameters improved by the application of a white light continuum generated in CaF2 *Opt. Commun.* **194** 443–8

[63] Riedel R, Stephanides A, Prandolini M J, Gronloh B, Jungbluth B, Mans T and Tavella F 2014 Power scaling of supercontinuum seeded megahertz-repetition rate optical parametric chirped pulse amplifiers *Opt. Lett.* **39** 1422–4

[64] Pergament M, Kellert M, Kruse K, Wang J, Palmer G, Wissmann L, Wegner U and Lederer M J 2014 High power burst-mode optical parametric amplifier with arbitrary pulse selection *Opt. Express* **22** 22202–10

[65] Seifert F, Petrov V and Woerner M 1994 Solid-state laser system for the generation of midinfrared femtosecond pulses tunable from 3.3 to 10 μm *Opt. Lett.* **19** 2009–11

[66] Kaindl R A, Wurm M, Reimann K, Hamm P, Weiner A M and Woerner M 2000 Generation, shaping, and characterization of intense femtosecond pulses tunable from 3 to 20 μm *J. Opt. Soc. Am.* B **17** 2086–94

[67] Tzankov P, Fiebig T and Buchvarov I 2003 Tunable femtosecond pulses in the near-ultraviolet from ultrabroadband parametric amplification *Appl. Phys. Lett.* **82** 517–9

[68] Baum P, Lochbrunner S and Riedle E 2004 Tunable sub-10 fs ultraviolet pulses generated by achromatic frequency doubling *Opt. Lett.* **29** 1686–8

[69] Beutler M, Ghotbi M, Noack F, Brida D, Manzoni C and Cerullo G 2009 Generation of high-energy sub-20 fs pulses tunable in the 250–310 nm region by frequency doubling of a high-power noncollinear optical parametric amplifier *Opt. Lett.* **34** 710–2

[70] Varillas R B, Candeo A, Viola D, Garavelli M, De Silvestri S, Cerullo G and Manzoni C 2014 Microjoule-level, tunable sub-10 fs UV pulses by broadband sum-frequency generation *Opt. Lett.* **39** 3849–52

[71] Petrov V and Noack F 1996 Mid-infrared femtosecond optical parametric amplification in potassium niobate *Opt. Lett.* **21** 1576–8

[72] Rotermund F, Petrov V, Noack F, Wittmann M and Korn G 1999 Laser-diode-seeded operation of a femtosecond optical parametric amplifier with MgO:LiNbO3 and generation of 5-cycle pulses near 3 μm *J. Opt. Soc. Am.* B **16** 1539–45

[73] Andriukaitis G, Balčiūnas T,Ališauskas S, Pugžlys A, Baltuška A, Popmintchev T, Chen M-C, Murnane M M and Kapteyn H C 2011 90 GW peak power few-cycle mid-infrared pulses from an optical parametric amplifier *Opt. Lett.* **36** 2755–7

[74] Kozich V, Moguilevski A and Heyne K 2012 High energy femtosecond OPA pumped by 1030 nm Yb:KGW laser *Opt. Commun.* **285** 4515–8

[75] Malevich P *et al* 2013 High energy and average power femtosecond laser for driving mid-infrared optical parametric amplifiers *Opt. Lett.* **38** 2746–9

[76] Ishii N, Kaneshima K, Kanai T, Watanabe S and Itatani J 2015 Generation of ultrashort intense optical pulses at 1.6 m from a bismuth triborate-based optical parametric chirped pulse amplifier with carrier-envelope phase stabilization *J. Opt.* **17** 094001

[77] Budrinas R, Stanislauskas T and Varanavičius A 2015 Passively CEP-stabilized frontend for few cycle terawatt OPCPA system *J. Opt.* **17** 094008

[78] Baudisch M, Pires H, Ishizuki H, Taira T, Hemmer M and Biegert J 2015 Sub-4-optical-cycle, 340 MW peak power, high stability mid-IR source at 160 kHz *J. Opt.* **17** 094002

[79] Di Trapani P, Andreoni A, Solcia C, Foggi P, Danielius R, Dubietis A and Piskarskas A 1995 Matching of group velocities in three-wave parametric interaction with femtosecond pulses and application to traveling-wave generators *J. Opt. Soc. Am.* B **12** 2237–44

[80] Shirakawa A, Sakane I and Kobayashi T 1998 Pulse-front-matched optical parametric amplification for sub-10 fs pulse generation tunable in the visible and near infrared *Opt. Lett.* **23** 1292–4

[81] Bor Z and Rácz B 1985 Group velocity dispersion in prisms and its application to pulse compression and travelling-wave excitation *Opt. Commun.* **54** 165–70

[82] Tzankov P, Zheng J, Mero M, Polli D, Manzoni C and Cerullo G 2006 300 μJ noncollinear optical parametric

amplifier in the visible at 1 kHz repetition rate *Opt. Lett.* **31** 3629–31

[83] Liebel M, Schnedermann C and Kukura P 2014 Sub-10 fs pulses tunable from 480 to 980 nm from a NOPA pumped by an Yb:KGW source *Opt. Lett.* **39** 4112–5

[84] Baltuška A, Fuji T and Kobayashi T 2002 Visible pulse compression to 4 fs by optical parametric amplification and programmable dispersion control *Opt. Lett.* **27** 306–8

[85] Schmidt C, Bühler J, Heinrich A-C, Leitenstorfer A and Brida D 2015 Noncollinear parametric amplification in the near-infrared based on Type-II phase matching *J. Opt.* **17** 094003

[86] Nikogosyan D N 1991 Beta barium borate (BBO) *Appl. Phys.* A **52** 359–68

[87] Ghotbi M, Ebrahim-Zadeh M, Petrov V, Tzankov P and Noack F 2006 Efficient 1 kHz femtosecond optical parametric amplification in BiB3O6 pumped at 800 nm *Opt. Express* **14** 10621–6

[88] Hellwig H, Liebertz J and Bohatý L 2000 Linear optical properties of the monoclinic bismuth borate BiB3O6 *J. Appl. Phys.* **88** 240–4

[89] Hellwig H, Liebertz J and Bohatý L 1998 Exceptional large nonlinear optical coefficients in the monoclinic bismuth borate BiB3O6 (BIBO) *Solid State Commun.* **109** 249–51

[90] Chen C, Wu Y, Jiang A, Wu B, You G, Li R and Lin S 1989 New nonlinear-optical crystal: LiB$_3$O$_5$ *J. Opt. Soc. Am.* B **6** 616–21

[91] Borsutzky A, Brünger R, Huang C and Wallenstein R 1991 Harmonic and sum-frequency generation of pulsed laser radiation in BBO, LBO, and KD*P *Appl. Phys.* B **52** 55–62

[92] Dorrer C, Consentino A, Irwin D, Qiao J and Zuegel J D 2015 OPCPA front end and contrast optimization for the OMEGA EP kilojoule, picosecond laser *J. Opt.* **17** 094007

[93] Becker P 1998 Borate materials in nonlinear optics *Adv. Mater.* **10** 979–92

[94] Kemlin V, Jegouso D, Debray J, Segonds P, Boulanger B, Menaert B, Ishizuki H and Taira T 2013 Widely tunable optical parametric oscillator in a 5 mm thick 5% MgO:PPLN partial cylinder *Opt. Lett.* **38** 860–2

[95] Lai C-J *et al* 2015 Multi-mJ mid-infrared kHz OPCPA and Yb-doped pump lasers for tabletop coherent soft x-ray generation *J. Opt.* **17** 094009

[96] Treacy E B 1969 Optical pulse compression with diffraction gratings *IEEE J. Quantum Electron.* **QE-5** 454–8

[97] Martinez O E, Gordon J P and Fork R L 1984 Negative group-velocity dispersion using refraction *J. Opt. Soc. Am.* A **1** 1003–6

[98] Fork R L, Martinez O E and Gordon J P 1984 Negative dispersion using pairs of prisms *Opt. Lett.* **9** 150–2

[99] Szipöcs R, Spielmann C, Krausz F and Ferencz K 1994 Chirped multilayer coatings for broadband dispersion control in femtosecond lasers *Opt. Lett.* **19** 201–3

[100] Kärtner F X, Matuschek N, Schibli T, Keller U, Haus H A, Heine C, Morf R, Scheuer V, Tilsch M and Tschudi T 1997 Design and fabrication of double-chirped mirrors *Opt. Lett.* **22** 831–3

[101] Zavelani-Rossi M, Cerullo G, De Silvestri S, Gallmann L, Matuschek N, Steinmeyer G, Keller U, Angelow G, Scheuer V and Tschudi T 2001 Pulse compression over a 170 THz bandwidth in the visible by use of only chirped mirrors *Opt. Lett.* **26** 1155–7

[102] Weiner A M 2000 Femtosecond pulse shaping using spatial light modulators *Rev. Sci. Instrum.* **71** 1929–60

[103] Binhammer T, Rittweger E, Ell R, Kartner F X and Morgner U 2005 Prism-based pulse shaper for octave spanning spectra *IEEE J. Quantum Electron.* **41** 1552–7

[104] Dugan M A, Tull J X and Warren W S 1997 High-resolution acousto-optic shaping of unamplified and amplified femtosecond laser pulses *J. Opt. Soc. Am.* B **14** 2348–58

[105] Zeek E, Maginnis K, Backus S, Russek U, Murnane M, Mourou G, Kapteyn H and Vdovin G 1999 Pulse compression by use of deformable mirrors *Opt. Lett.* **24** 493–5

[106] Verluise F, Laude V, Cheng Z, Spielmann Ch and Tournois P 2000 Amplitude and phase control of ultrashort pulses by use of an acousto-optic programmable dispersive filter: pulse compression and shaping *Opt. Lett.* **25** 575–7

[107] Steinle T, Kedenburg S, Steinmann A and Giessen H 2014 Combining cw-seeding with highly nonlinear fibers in a broadly tunable femtosecond optical parametric amplifier at 42 MHz *Opt. Lett.* **39** 4851–4

[108] Rothhardt J, Demmler S, Hädrich S, Peschel T, Limpert J and Tünnermann A 2013 Thermal effects in high average power optical parametric amplifiers *Opt. Lett.* **38** 763–5

[109] Kleinman D A 1962 Nonlinear dielectric polarization in optical media *Phys. Rev.* **126** 1977–9

[110] Armstrong D J, Alford W J, Raymond T D and Smith A V 1996 Absolute measurement of the effective nonlinearities of KTP and BBO crystals by optical parametric amplification *Appl. Opt.* **35** 2032–40